

A STATISTICAL STUDY OF MASSIVE CLUSTER-FORMING CLUMPS

TOMOMI SHIMOIKURA¹, KAZUHIITO DOBASHI¹, FUMITAKA NAKAMURA^{2,3}, TOMOAKI MATSUMOTO⁴, AND TOMOYA HIROTA^{2,3}
¹ ikura@u-gakugei.ac.jp

¹Department of Astronomy and Earth Sciences, Tokyo Gakugei University, Koganei, Tokyo 184-8501, Japan

²National Astronomical Observatory of Japan, Mitaka, Tokyo 181-8588, Japan

³Department of Astronomical Science, School of Physical Science, SOKENDAI (The Graduate University for Advanced Studies), Osawa, Mitaka, Tokyo 181-8588, Japan

⁴Faculty of Sustainability Studies, Hosei University, Fujimi, Chiyoda-ku, Tokyo 102-8160, Japan

ABSTRACT

We report results of the observations of 15 regions in several molecular lines for a statistical study of massive cluster-forming clumps. We identified 24 clumps based on the C¹⁸O ($J = 1 - 0$) data obtained by the NRO 45 m telescope, and found that 16 of them are associated with young clusters. The clumps associated with clusters have a typical mass, radius, and molecular density of $\sim 1 \times 10^3 M_{\odot}$, ~ 0.5 pc, $\sim 1 \times 10^5 \text{ cm}^{-3}$, respectively. We categorized the clumps and clusters into four types according to the spatial coincidence of gas and star density, and discussed their evolutions: Clumps without clusters (Type 1), clumps showing good correlations with clusters (Type 2), clumps showing poor correlations with clusters (Type 3), and clusters with no associated clumps (Type 4). Analyses of the velocity structures and the chemical compositions imply that the clump + cluster systems should evolve from Type 1 to Type 4. We found that some of the Type 2 clumps are infalling on the clump-scale to form clusters at the clump center, which should commonly occur in the beginning of cluster formation. Interestingly, all of the identified Type 1 clumps are likely to be older than the Type 2 clumps in terms of chemical compositions, suggesting that they have been gravitationally stable for a long time possibly being supported by the strong magnetic field of $\gtrsim 1$ mG. Type 1 clumps younger than the observed Type 2 clumps should be very rare to find because of their short lifetime.

Keywords: ISM: molecules–ISM:clouds–stars: formation, cluster-forming clump

1. INTRODUCTION

Young clusters with ages of a few Myr are deeply embedded in their natal molecular clumps. These clusters can be easily identified in near-infrared images, and we call such young clusters IR clusters. Although it is well known that stars are often born in clusters (e.g., Lada & Lada 2003; Gutermuth et al. 2009), formation and evolution processes of clusters still remain unclear. Observational studies of IR clusters and their natal clumps provide a key to understand the formation and evolution of clusters and their environments.

Cluster-forming clumps tend to exhibit complex velocity structures with multiple velocity components. Several hypotheses have been proposed to explain the velocity fields of cluster-forming clumps: For example, it is possible that the clumps can be affected by an expanding H II region (e.g., Shimoikura et al. 2015) or by collisions of smaller clumps and/or filaments (e.g., Higuchi et al. 2009; Dobashi et al. 2014). Peretto et al. (2006, 2007) found two velocity components in the massive cluster-

forming clump NGC2264C, for which they suggested a large-scale collapsing motion of the clump. Similarly, we investigated the velocity structure of the cluster-forming clump S235AB, and found that the entire clump is infalling with rotation toward the clump center where the most massive star in the cluster is forming (Shimoikura et al. 2016).

How the velocity structures of the natal clumps evolve along with the cluster formation? Considering the results we obtained for the clump S235AB (Shimoikura et al. 2016), we would expect that the clumps forming IR clusters should experience the clump-scale infalling motion with rotation in an early stage of cluster formation. In order to confirm if such a dynamical infall is a common phenomenon for the cluster-forming clumps, we need to carry out a statistical study with a rich sample of massive clumps with young clusters.

We also note the fact that there is a large variation in morphologies of the IR clusters and their natal clumps, which is believed to represent various evolutionary stages of cluster formation (e.g., Lada & Lada

2003). However, the quantitative relationships between the properties of clusters (e.g., age, size, number of constituent stars) and their natal clumps (e.g., mass, density, and velocity dispersion) still remain unclear. The relationships should change along with the evolution time, but it is generally difficult to assess the absolute ages of the natal clumps. There are, however, some molecules (e.g., CCS) for which the time variations of the abundances have been calculated (e.g. Suzuki et al. 1992), and they can be used as a measure of the clump ages. In order to study the relationships between the clusters and natal clumps, it is therefore very important to investigate systematically not only the physical properties but also the chemical compositions of the clumps.

In this study, we conducted systematic observations of 15 dust condensations selected from a catalog of dust condensations compiled by Dobashi (2011). We used the NRO 45 m telescope to observe the dust condensations with different tracers.

In the $C^{18}O$ data from the 45 m telescope, the condensations can be divided into smaller clumps. In one of the clumps named S235AB corresponding to No.4423 in the 15 dust condensations, we detected the global infalling motion with rotation as mentioned in the above. We show the results for S235AB in detailed in a separate paper (Shimoikura et al. 2016). In this paper, we present the results for all of the clumps we identified.

Our primary goals in this paper are (i) to find differences between the clumps with and without IR clusters and to investigate how and under what physical conditions the cluster formation can occur mainly by using the $C^{18}O$ data as a tracer of kinematics, and (ii) to infer the evolutionary stages of the clumps by comparing the abundances of CCS and HC_3N as well as those of CS and SO. As the CCS emission has been detected only in dark clouds (e.g., Nakamura et al. 2014) but not in active cluster-forming clumps (e.g., Lai & Crutcher 2000; Shimoikura et al. 2015), we are particularly interested in carrying out a CCS survey for our targets.

This paper is organized as follows. In Section 2, we describe the targets selected for the observations. We also describe our observations using the 45 m radio telescope. We identify 24 molecular clumps using the $C^{18}O$ ($J = 1 - 0$) data and derive their physical properties in Section 3. We analyze the chemical compositions and velocity structures of the clumps, and discuss how the clumps should evolve in Section 4. We present the summary of this paper in Section 5.

2. OBSERVATIONS

2.1. The Target Dust Condensations

Based on the catalog of dust condensations of Dobashi (2011) and Dobashi et al. (2013), we selected 15 dust

condensations. Extinction maps of the 15 dust condensations selected for this study are shown in Figure 1. Numbers in the figure correspond to the condensation numbers given by Dobashi (2011). Except for No. 4678, the dust condensations we selected for the observations are regarded to include IR clusters by Dobashi (2011, and assigned Flag ‘3’ in their catalog), i.e., the dust condensations appear as a ‘hole’ in the A_J map due to the increase of star density compared to adjacent regions, but as a ‘bump’ in the $E(J - H)$ map because of the intrinsically red colors of young stars. We selected the 15 dust condensations from various star forming regions within 2.4 kpc from the Sun. Except for No. 4398¹, the distances to the condensations were obtained from the literature. We selected relatively massive condensations observable from Nobeyama with a mass of greater than $100M_{\odot}$ except for No.4059 ($\sim 50 M_{\odot}$)².

Ten of the dust condensations are associated with known IR clusters in active cluster-forming regions such as S201 and Mon R2 (e.g., Bica et al. 2003a,b; Kirsanova et al. 2008). Typical ages of the IR clusters are 1 – 5 Myr. We also conducted our own analyses using the 2MASS Point Source Catalog (PSC) to reveal the star density distribution around the selected condensations, which is described in detail in Section 3.4. Based on the analyses, we found that the rest of the 5 dust condensations are not associated with any apparent IR clusters. The selected dust condensations and their main characteristics are summarized in Table 1.

2.2. Observations with the NRO 45 m Telescope

The mapping observations of the 15 dust condensations using the NRO 45 m telescope were carried out during two separate observing periods. All of the observations were performed in the on-the-fly (OTF) mode. The observed molecular lines and the resulting noise levels for each line are summarized in Table 2.

2.2.1. Observations of ^{12}CO , ^{13}CO , $C^{18}O$, CS, SO and $C^{34}S$

¹ For this region, we calculated the kinematic distance by ourselves using the Galactic rotation models in the literature (Kerr & Lynden-Bell 1986; Wouterloot & Brand 1989; Wouterloot et al. 1990). We used the observed ^{13}CO peak radial velocity $V_{LSR} = -2.2 \text{ km s}^{-1}$, $R_0 = 8.5 \text{ kpc}$, and $\Theta_0 = 220 \text{ km s}^{-1}$, where Θ_0 is the rotational speed of the Galaxy at R_0 . We obtained a kinematic distance of 0.81 kpc which corresponds to the “far” distance in the model.

² For the mass estimation, we used near-infrared (NIR) color excess map of $E(J - H)$ for the 15 dust condensations from Dobashi (2011). We transformed the extinction values to hydrogen column densities using the relations $N[HI+H_2] = 5.8 \times 10^{21} E(B - V) \text{ cm}^{-2} \text{ mag}^{-1}$ (Bohlin et al. 1978) with $R_V = A_V / E(B - V) = 3.1$ (Cardelli et al. 1989) and $A_V = E(J - H) / 0.107$ (Rieke & Lebofsky 1985). We then calculated the total mass of the dust condensation as the sum of the extinction values above $A_V = 1 \text{ mag}$.

Observations of the 15 dust condensations with six emission lines at 100 GHz (^{12}CO , ^{13}CO , C^{18}O , CS, SO and C^{34}S) were conducted for 10 days in February 2013. The beam size of the telescope is $\sim 15''$ at 110 GHz. The single-beam two-polarization two-sideband-separation (2SB) sideband-separating Superconductor-Insulator-Superconductor (SIS) receiver TZ (Asayama & Nakajima 2013) was used as the frontend, and the digital spectrometer SAM45 with 4096 channels covering a total band width of 31 MHz and a velocity resolution of $\sim 0.02 \text{ km s}^{-1}$ was used as the backend. The overall system temperature (T_{sys}) typically ranged from 150 K to 300 K.

During the first part of the observations, the receiver was tuned to the ^{12}CO ($J = 1 - 0$) line, and $\sim 6' \times 6'$ mapping observations centered on each of the dust condensations were performed along the equatorial coordinates to investigate the molecular distributions. Afterward, the receiver was tuned to the ^{13}CO , C^{18}O , CS, SO, and C^{34}S lines to perform simultaneous $\sim 5' \times 5'$ mapping observations centered on the same peaks as those for the ^{12}CO observations.

An ambient-temperature chopper wheel was employed to determine the antenna temperature scale. The telescope pointing for each region was checked every 1.5 hours using SiO maser sources at 43 GHz, ensuring that the pointing remained accurate within $\sim 3''$. The sideband ratios of the receiver at the rest frequencies of the observed molecular lines were also checked everyday to further calibrate the spectral data, which fluctuated within $\sim 10\%$ each time the receiver was tuned. Calibration was also checked by taking the average spectra of the central $100'' \times 100''$ of the dust condensation No. 4423 for all of the molecular lines, confirming consistent calibration within 10% error.

The baselines of the spectral data were removed by fitting the emission-free velocity ranges with linear functions, and the data were converted into three-dimensional data with a spheroidal convolution at a angular grid size of $7''.5$ using the software package

Software: NOSTAR, (Sawada et al. 2008). The data were then corrected for the main-beam efficiency of the telescope into the T_{mb} scale for which main beam efficiencies (η_{mb}) were assumed to be 0.27, 0.30, 0.30, 0.37, 0.38, and 0.39 for the ^{12}CO , ^{13}CO , C^{18}O , CS, SO and C^{34}S lines, respectively.

We finally obtained the spectral data with an effective angular resolution of approximately $22'' - 24''$ and a velocity resolution of 0.05 km s^{-1} for each emission line. The typical 1σ noise level in the ^{12}CO spectra was $\Delta T_{\text{mb}} = 1.2 \text{ K}$, and $\Delta T_{\text{mb}} = 0.2 - 0.5 \text{ K}$ for the other lines.

2.2.2. Observations of CCS and HC_3N

Observations of the 15 dust condensations were also carried out with the CCS and HC_3N emission lines at 45 GHz using the NRO 45 m telescope for three days in March 2017. We obtained $\sim 5' \times 5'$ maps for the 15 dust condensations in both of the lines simultaneously, covering the same areas as for the 100 GHz observations. The dual-polarization receiver Z45 (Nakamura et al. 2015) was used, which provided $T_{\text{sys}} \simeq 160 \text{ K}$. Spectral data were obtained with the 4096 channels using the SAM45 spectrometer operating at a resolution of 0.1 km s^{-1} . At 45 GHz, the beam size of the telescope was $\sim 37''$ and η_{mb} was 0.7.

The telescope pointing and data reduction were performed in the same manner used for the 100 GHz observations. We smoothed the obtained spectral data to an effective angular and velocity resolutions of $\sim 49''$ and 0.2 km s^{-1} , respectively. The resulting 1σ noise level is $\Delta T_{\text{mb}} \simeq 0.2 \text{ K}$ for these resolutions.

3. RESULTS

3.1. Identification of Molecular Clumps and Estimation of their Physical Properties

Figures 2–7 show integrated intensity maps of the molecular emission lines observed with the 45 m telescope. In the figures, only molecular lines significantly detected at the 3σ noise level are shown. It is seen that the C^{18}O line was detected in all of the target regions, although some lines such as C^{34}S , CCS, and HC_3N were not detected in some of the dust condensations, especially in those without IR clusters (e.g., No. 4398 in Figure 5).

Based mainly on the C^{18}O data, we identified molecular clumps and estimated their physical parameters. We used the following four-steps procedure to define the molecular clumps in this study:

1. We first searched for pixels having intensities greater than the 3σ noise level in the C^{18}O intensity map, and regarded a set of continuous pixels as a clump.
2. We then searched for the peak intensity position in each clump, and defined S the surface area of the clump as the region enclosed by the contour at the 50% of the peak intensity.
3. In the above step 2, we found that four clumps (Nos. 3645, 3890, 4417, and 4565) have two local peaks within S each of which is well separated from the other peak in other molecular lines such as SO and/or CS. In addition, the two local peaks have different radial velocities separated by $> 0.5 \text{ km s}^{-1}$. We believe that the two local peaks should

originate from two distinct clumps lying along the same line-of-sight. We therefore divided each of the four clumps into two smaller clumps at the valley in the C^{18}O contours, and re-measured S for the smaller clumps in the same way as described in the step 2.

4. Among the clumps selected by the above steps, we chose only the clumps having S greater than 0.3 arcmin² (corresponding to 20 pixels in the C^{18}O intensity maps) to analyze in this paper in order to ensure the definite detection.

Using the above procedure, we identified 24 clumps in total in the observed 15 dust condensations. We refer to the clumps as 3645a, 3645b, and so on, in the order of increasing right ascension.

To examine the star-formation activity in the clumps, we investigated the young stellar objects (YSOs) associated with each clump. The YSOs were searched for by referring to the catalogs of *IRAS* point sources. Eleven clumps were found to be associated with one YSO selected from the *IRAS* catalog based on the selection criteria proposed by Dobashi et al. (1994), and they have a bolometric luminosity greater than $10^2 L_\odot$.

In the following, we estimate physical parameters of the individual clumps. To derive column densities from the observed emission lines, we assumed the local thermodynamic equilibrium (LTE). Details of the derivations are described in Appendix A. Based on the ^{12}CO data, we calculated excitation temperature T_{ex} at the individual positions of each clump for the observed emission lines. Using Equation (A1) and assuming that the ^{12}CO emission line is optically thick ($\tau \gg 1$), T_{ex} can be derived as

$$T_{\text{ex}} = 5.53 \left\{ \ln \left[1 + \frac{5.53}{T_{\text{mb}}^{\text{co}} + 0.819} \right] \right\}^{-1} \text{ K}, \quad (1)$$

where $T_{\text{mb}}^{\text{co}}$ is the peak brightness temperature in K of the ^{12}CO data estimated by a single Gaussian fit at the individual observed positions. The maximum T_{ex} for each clump ranges from 28.0 K (clump 4059) to 82.1 K (clump 4974), and the average T_{ex} within S , \bar{T}_{ex} , ranges from 24.5 K (clump 4059) to 59.4 K (clump 4974).

Using Equation (A2) and the derived values of T_{ex} , we calculated the column densities of C^{18}O , SO, CS, and C^{34}S of the clumps on the assumption of LTE and the optically thin cases ($\tau \ll 1$).

The molecular hydrogen column density $N(\text{H}_2)$ was derived from the C^{18}O column density $N(\text{C}^{18}\text{O})$ by assuming the relation $N(\text{C}^{18}\text{O}) = 1.7 \times 10^{-7} N(\text{H}_2)$ (Frerking et al. 1982). The LTE mass of the clumps within S , M_{LTE} , was derived as

$$M_{\text{LTE}} = \bar{\mu} m_{\text{H}} \int_S N(\text{H}_2) dS, \quad (2)$$

where m_{H} is the hydrogen mass, and $\bar{\mu}$ is the mean molecular weight, which is assumed to be 2.8. The mean volume density in the clumps, $n(\text{H}_2)$, was estimated by dividing M_{LTE} by the clump volume $V = (4/3)\pi R^3$ where R is the radius of the clump defined as $R = \sqrt{S/\pi}$.

We also calculated the virial mass, M_{vir} , as

$$M_{\text{vir}} = \frac{5R}{G} \frac{\overline{\Delta V}(\text{C}^{18}\text{O})^2}{8 \ln 2}, \quad (3)$$

where G is the gravitational constant, and $\overline{\Delta V}(\text{C}^{18}\text{O})$ is the mean line width (FWHM) in the composite profile obtained by averaging all of the spectra of the clump within S . We further derived the average fractional abundances of SO, CS, and C^{34}S within S by estimating the column densities and dividing them by $N(\text{H}_2)$ derived from the C^{18}O data.

Using this approach, we found that the clumps have sizes ranging from 0.1 to 0.6 pc, masses ranging from 5 to 4397 M_\odot , and volume densities ranging from 1.2×10^4 to $1.9 \times 10^5 \text{ cm}^{-3}$. These physical properties are summarized in Table 3.

We note that the ^{12}CO spectra at some positions around the peak intensities in the clumps 3890a, 4423a, 4753a, and 4974 are optically thick and suffer from self-absorption. For these positions, we cannot determine T_{ex} precisely, which is a source of uncertainty in our mass estimates. Here we compare our estimates with those in the literature. Sakai et al. (2006) estimated the LTE mass of clump 3890b (which they called AFGL333 core A) to be $2300 M_\odot$ based on the C^{18}O data obtained with the NRO 45 m telescope and assuming a uniform T_{ex} of 20 K. For the same clump, we estimated $4000 M_\odot$ at their assumed distance of 1950 pc, $\sim 70\%$ larger than their value. As another example, Peretto et al. (2006) derived a mass of $1650 M_\odot$ for clump 4753b (NGC2264C) using 1.2 mm continuum data, assuming a dust temperature of 15 K. Our value for the same clump would be rescaled to $1400 M_\odot$ at their assumed distance of 800 pc, which is $\sim 20\%$ smaller than their value. We found that these differences are mainly due to the difference of the adopted T_{ex} and the definition of the surface areas of the clumps.

We also derived fractional abundances of the CCS and HC_3N molecules of the clumps. The CCS emission was found only in four clumps (3890a, 4753a, 4753b, and 4974), whereas the HC_3N emission was found in nine clumps (3645b, 3890a, 3890b, 3921, 4423a, 4565b, 4753a, 4753b, and 4974). All of the clumps detected in CCS were detected also in HC_3N . At an rms noise level of $0.1 - 0.2 \text{ K}$ and a resolution of 0.2 km s^{-1} , there was no detection of both CCS and HC_3N in the other 15 clumps.

For the nine clumps detected in CCS and/or HC_3N ,

the emission lines were detected only in compact regions in the clumps, and their peak positions in the integrated intensity maps do not match with those of the C^{18}O line. Therefore, we decided to derive physical properties using these lines at the HC_3N intensity peak positions. To derive the column densities of CCS and HC_3N of the clumps, $N(\text{CCS})$ and $N(\text{HC}_3\text{N})$, we tried to estimate T_{ex} by fitting three main hyperfine components of the HC_3N spectra. However, we could not fit the spectra well because of the low signal-to-noise ratios. We therefore derived $N(\text{CCS})$ and $N(\text{HC}_3\text{N})$ using Equation (A2) on the assumption of a uniform T_{ex} of 5 K measured in dark clouds (e.g., Hirota et al. 2009) as well as much higher T_{ex} ($\simeq 34 - 66$ K) measured from the ^{12}CO spectra, which should give the lower and upper limits of the column densities, respectively. We then smoothed the C^{18}O spectrum at the HC_3N peak position of each clump to $49''$, the same resolution as at 45 GHz, and derived $N(\text{H}_2)$ from the smoothed C^{18}O spectrum in the same manner as for deriving the clump masses. Finally, we derived the fractional abundances of CCS and HC_3N of the clumps, $f(\text{CCS})$ and $f(\text{HC}_3\text{N})$, by dividing their column densities by $N(\text{H}_2)$. The range of $f(\text{CCS})$ in the four clumps lies between 0.5×10^{-10} and 4.1×10^{-10} , and that of $f(\text{HC}_3\text{N})$ in the nine clumps lies between 0.4×10^{-10} and 6.2×10^{-10} . For the clumps detected in HC_3N but not in CCS, we derived the upper limits of $N(\text{CCS})$ and $f(\text{CCS})$ from the noise levels to be $< 1 \times 10^{12} \text{ cm}^{-2}$ and $< 1 \times 10^{-11}$, respectively. The derived column densities and fractional abundances for the nine clumps are shown in Table 4.

We note that $f(\text{CCS})$, $f(\text{HC}_3\text{N})$, $f(\text{CS})$, and $f(\text{SO})$ derived in the above may be overestimated, because we derived $N(\text{H}_2)$ from $N(\text{C}^{18}\text{O})$ assuming their flat ratios. In very dense regions, C^{18}O can be less abundant due to adsorption onto dust grains (e.g., Bergin et al. 2002) or due to selective destruction by the strong UV radiation from young massive stars (e.g., Shimajiri et al. 2014), which may cause an underestimation of $N(\text{H}_2)$. Taking into account all of the uncertainties in distance, T_{ex} , and $N(\text{H}_2)$, we conclude that our estimates of mass and fractional abundances for the 24 clumps have an uncertainty of 50% at most.

3.2. Velocity Dispersion of the Clumps

We investigated the velocity dispersion of the clumps. The velocity dispersion σ_{obs} of the observed emission lines at each observed position was derived as

$$\sigma_{\text{obs}} = \sqrt{\frac{\int (V - V_0)^2 T_{\text{mb}} dV}{\int T_{\text{mb}} dV}} \quad (4)$$

where V_0 is the intensity-weighted mean velocity measured as $V_0 = \int V T_{\text{mb}} dV / \int T_{\text{mb}} dV$.

Based on the C^{18}O data, we derived σ_{obs} of the emission line, $\sigma_{\text{obs}(\text{C}^{18}\text{O})}$, from the above equation. We regard that $\sigma_{\text{obs}(\text{C}^{18}\text{O})}$ consists of the thermal (σ_{therm}) and non-thermal (σ_{NT}) components (e.g., Myers 1983), and can be expressed as

$$\sigma_{\text{obs}(\text{C}^{18}\text{O})}^2 = \sigma_{\text{therm}}^2 + \sigma_{\text{NT}}^2 + \sigma_{\text{reso}}^2. \quad (5)$$

Here, $\sigma_{\text{reso}} (= 0.05 \text{ km s}^{-1})$ is the velocity resolution of the data, and σ_{therm} can be calculated as

$$\sigma_{\text{therm}} = \sqrt{\frac{kT_{\text{ex}}}{\mu(\text{C}^{18}\text{O})m_{\text{H}}}} \quad (6)$$

where $\mu(\text{C}^{18}\text{O})$ is the mean molecular weight of C^{18}O ($=30$). The three-dimensional velocity dispersion of turbulence at each position can be estimated as $\sigma_{3\text{D}} = \sqrt{3}\sigma_{\text{NT}}$. The mean values of $\sigma_{\text{obs}(\text{C}^{18}\text{O})}$, σ_{therm} , and $\sigma_{3\text{D}}$ for each clump averaged within the clump surface S are listed in Table 5.

3.3. Search for Outflows

We investigated the presence of molecular outflows associated with the clumps by searching for high-velocity wings in the ^{12}CO spectra. The procedure is explained in Appendix B. We also searched for molecular outflows associated with the clumps in the literatures (e.g., Wu et al. 2004). As a result, we found nine outflows in the 24 clumps in total, and two of the outflows which are associated with clumps 4417a and 4417c are newly identified by this study. We show the locations of the nine outflows in Figure 8, and summarize their properties in Table 6.

For clump 4753a (NGC2264D), Buckle et al. (2012) identified multiple blue and redshifted lobes through ^{12}CO ($J = 3 - 2$) observations. Our map for this clump does not cover the full extent of the red outflow lobe, and only the blue lobe is seen in Figure 8. We therefore list properties of only the blue lobe for this clump in Table 6.

For clump 3921 (AFGL4029), Snell et al. (1988) found the total outflow lobe mass (the sum of the masses of the red and blue lobes) to be $9.7 M_{\odot}$ using ^{12}CO . Their outflow mass differs significantly from our value of $44.1 M_{\odot}$ (the lower limit), which is likely to be explained mainly by their different assumed value of T_{ex} ($=25$ K).

We compared the distributions of the molecular outflows with the locations of the IR clusters, and found that some of the outflows coincide well with the IR clusters (see Figure 8). Although the identified outflow lobes of clumps 3890a and 4417a are likely to be unrelated to the corresponding clusters, outflow lobes in the other clumps (i.e., clumps 4423a and 4974) coincide well with the positions of the clusters. In the maps of Dierickx et al. (2015) produced from their SMA observations,

clump 4974 (Mon R2) shows the presence of 11 CO outflows in the innermost $\sim 1'$ region around the cluster. Though only one pair of red and blue lobes is seen in our map, it is likely that our maps trace the entirety of the high velocity flow originating from the cluster.

3.4. Search for IR Clusters Based on the 2MASS Data and Estimation of the Physical Properties

The 2MASS PSC was used to systematically search for IR clusters associated with all of the 24 observed clumps. We selected a $15' \times 15'$ region around each clump except for the clump 4974³, and produced star density maps of the regions to identify clusters using stars which are not recorded as ‘minor planets’ in the 2MASS PSC. We will explain the reason why we selected the stars in this way in Appendix C.

The star density map of each cluster was constructed by counting the number of stars in a 0.4 radius from each $7''.5$ grid set along the equatorial coordinates. The obtained star density maps still contained contributions from the background sources. To estimate the properties of the clusters, we obtained final star density maps free from the background using the 3σ clipping procedure described in detail by Shimoikura et al. (2013). The resulting 1σ noise level of the star density maps is in the range of 3–5 stars arcmin⁻².

We searched for pixels in the star density maps with a density greater than the 4σ noise level for each region, and regarded them as IR clusters. We then defined the extents of the clusters by the contour drawn at the 30% level of the peaks. As a result, we identified 23 IR clusters within the 24 clumps. Nineteen of the IR clusters have been previously identified in other studies. In addition to these, we newly identified three IR clusters associated with the dust condensation No. 3890. Distribution of the identified IR clusters in the area observed with the 45 m telescope is shown in the last panel of Figures 2–7, in which the WISE 3.4 μ m image (Wright et al. 2010) is overlaid to see the extended emission associated with the clumps or the IR clusters. In each panel, the IR clusters are labeled 3645cl, 3890cl1, 3890cl2, etc. In summary, the observed regions contain 24 molecular clumps, and 16 of them are associated with at least one

IR cluster, whereas the other eight clumps are associated with no apparent IR cluster. Among the 23 clusters identified, six are not associated with any particular clumps.

To derive properties of the IR clusters, we first defined their radius as $R_\star = \sqrt{S_\star/\pi}$ where S_\star is the surface area of the clusters defined at the 30% contour level. We then investigated the cumulative number of stars for each cluster, $N_\star(r)$, as a function of distance r from the cluster center. An example of the results is shown in Figure 9. We found that $N_\star(r)$ increases rapidly with r and becomes rather flat at $r \simeq 2R_\star - 4R_\star$, and then diverge at larger r due to counting uncertainty, which is the same tendency that we already found in other cluster-forming regions (Shimoikura et al. 2013).

We defined the total number of stars contained in an IR cluster, N_\star , as the average value of $N_\star(r)$ in the flattened part of the $N_\star(r)$ vs. r diagram. For most of the clusters, we defined N_\star as the average value in the range $2R_\star < r < 3R_\star$. For clusters 3923cl and 4974cl, we decided to define N_\star in the range $4R_\star < r < 5R_\star$. We found that the N_\star varies in the range of 12 to 380, and R_\star varies from 0.12 to 0.76 pc. These parameters are summarized in Table 7.

The largest N_\star (= 380) in our sample is found in 4974cl which is a rich IR cluster in the Mon R2 region. The cluster has already been studied with the 2MASS data by Carpenter (2000) who estimated the total number of stars to be $N_\star = 371$ in an effective radius of ~ 1.85 pc based on the Wainscoat model (Wainscoat et al. 1992). We found that their value for N_\star is found to be quite close to ours.

Several studies have used NIR data to derive the structural parameters of clusters by fitting the star density profiles with the King’s model (King 1962). Although we attempted to fit the star density of the identified IR clusters with the King model, most of the clusters could not be fitted well owing to their complex morphologies. The 23 clusters studied here have a wide variety of structures, and some of them show multiple peaks. Camargo et al. (2011) studied eight IR clusters among those we study here (clusters 4417cl1–cl4 and 4423cl1–cl4) using the 2MASS PSC and the King model, but they could successfully fit only two of them (4417cl1 and 4417cl3 that they call ‘Sh2-235 Cluster’ and ‘Sh2-235 East2’, respectively).

Lada & Lada (2003) suggested that there are two morphological types of cluster structures, hierarchical and concentrated, and that these structures may reflect the physical processes responsible for cluster formation. We found that most of our identified clusters are not spherical except for six clusters not associated with any particular clumps. For example, cluster 3890cl2, which is located in a cavity of C¹⁸O gas, has a spherical mor-

³ We investigated how the number of stars in the clusters N_\star of each of our targets changes depending on the survey window size. We investigated N_\star from the star density maps produced for the window size $10' \times 10'$, $15' \times 15'$, $20' \times 20'$, $30' \times 30'$, $40' \times 40'$, and $60' \times 60'$ using the stars except for those with a minor planet flag. As a result, we found that the value of N_\star changes depending on the window size only in the case of the cluster associated with the clump 4974. For this target, $N_\star=330$ for the size $15' \times 15'$, but $N_\star=380$ for the size $\gtrsim 40' \times 40'$. On the other hand, N_\star of the other clusters do not change for the window size $\gtrsim 15' \times 15'$, because their extents are small. We therefore selected a $40' \times 40'$ region around the clump 4974 to produce the star density map.

phology (see Figure 3). By contrast, cluster 4423cl2 is elliptical and matches well with its associated clump (see Figure 5). We measured the ratio of the minor and major axis with the 2D Gaussian fit for each cluster as shown in the last column of Table 7, and found that clusters associated with less molecular gas tend to be more spherical with a ratio of minor to major axis of > 0.8 , possibly suggesting that the more spherical clusters are older.

3.5. Relationships between Clumps and IR Clusters

By comparing the distributions of the clumps with those of the associated IR clusters (Figures 2–7), we found that their spatial coincidences vary from clump to clump. For example, in some cases, there are two clumps within the extent of one cluster (e.g., clusters 3645cl and 4565cl), while there are sometimes two IR clusters within the extent of one clump (e.g., clump 4753a). We also note that the IR clusters in clump 3921 can be resolved by eye into two IR clusters, 3921cl1 and 3921cl2, and the former cluster is not associated with any molecular emission.

There have been some studies to investigate evolution of cluster forming clumps, e.g., by Ridge et al. (2003), Kawamura et al. (2009), Higuchi et al. (2009), and Shimoikura et al. (2013). In their studies, clumps are classified by eye inspection mainly according to the presence of the associated clusters and their morphological relations. To examine the relationship between the clumps and the IR clusters and to classify their morphological types more quantitatively, we investigated the spatial correlations between $N(\text{C}^{18}\text{O})$ and the star densities (SD) of the associated clusters for the 16 clumps. To do this, we re-gridded and smoothed the data sets to the same angular resolution ($48''$) and performed a linear least-square fit to quantify the $N(\text{H}_2)$ vs. SD relation. The results are shown in Figure 10. Correlation coefficients of the fit, r , ranges from 0.1 to 0.8.

To characterize the identified clumps and clusters in terms of the cluster formation, we classified them into four types according to the following correlation relationship:

1. We classify clumps associated with no apparent IR cluster as Type 1.
2. We classify clumps that are well-correlated with IR clusters with a correlation coefficient of $\gtrsim 0.5$ as Type 2. Such clumps have similar morphologies to the clusters.
3. We classify clumps not well-correlated with IR clusters with a correlation coefficient of < 0.5 as Type 3. In such clumps, the peaks of the star den-

sity of the IR clusters do not match with those of the clumps.

4. Finally, we classify clusters not associated with any clumps as Type 4.

Among the 24 clumps, eight, seven, and nine clumps are classified as Type 1, 2, and 3, respectively. In addition, six IR clusters are classified as Type 4. The classification of the clumps and IR clusters are summarized in Table 8.

3.6. Physical Properties of the Clumps

We investigated the correlations between the physical properties of the clumps using the derived parameters listed in Tables 3, 5, and 6.

Figure 11 shows the relations among M_{vir} , M_{LTE} , R , and ΔV for the clumps of Types 1, 2, and 3, which are shown in different colors. We also plotted the same relations for clumps identified in the S252, S247, and BFS52 regions using C^{18}O data presented by Shimoikura et al. (2013), which were also obtained with the NRO 45 m telescope. We classified these clumps into the three types (Types 1–3) in the same way as explained above.

As shown in Figure 11(a), many of the clumps have a mass of the same order as their virial masses, suggesting that they may be in the virial equilibrium. However, there is a tendency that masses of the massive clumps ($M_{\text{LTE}} \gtrsim 10^3 M_{\odot}$) are significantly higher than the virial masses. These clumps can be collapsing, if they are not supported by the clump-supporting forces such as the magnetic field. In fact, as we will show in Section 4.2, some of the Type 2 clumps are actually collapsing.

The relationship between M_{LTE} and R in Figure 11(b) reveals that the clumps have a molecular number density in the range $10^4 < n(\text{H}_2) < 10^5 \text{ cm}^{-3}$, which is consistent with the results of previous studies of cluster-forming clumps (e.g., Saito et al. 2007; Shimoikura et al. 2013).

In Figure 11(c), it is apparent that the clumps with clusters, particularly Type 2 clumps, have larger line widths than those without clusters. We also found that the clumps having large line widths are associated with outflows, suggesting that the outflows are supplying turbulence to the clumps.

It has been long suggested that outflows are an important source of turbulence of natal clumps (e.g., Snell et al. 1988; Nakamura & Li 2011). In order to see how much the outflows can contribute to the observed turbulence, we estimated the dissipation rates of turbulence of the clumps as $\dot{P}_{\text{turb}} = -0.21 M_{\text{LTE}} \sigma_{3\text{D}}^2 / R$ (Nakamura & Li 2014, see their equations 4 and 5) using parameters in Tables 3 and 5, and compared them with \dot{P}_{flow} the ejection rates of momentum of the outflows in Table 6.

Results are shown in Figure 12. For \dot{P}_{flow} , we plotted the geometrical mean values with error bars representing the minimum and maximum estimates (see Appendix B). As seen in the figure, \dot{P}_{flow} is comparable to or larger than \dot{P}_{turb} for all of the Type 2 and 3 clumps within the errors, suggesting that the observed turbulence can be maintained by the outflows for these clumps. For the Type 1 clump (3890a), however, \dot{P}_{flow} is significantly smaller than \dot{P}_{turb} , and thus the observed turbulence of this clump should dissipate on a scale of crossing time ($R/\sigma_{3D} \simeq 3.8 \times 10^5$ yr), if the clump does not form additional outflows in the future.

Figure 11 suggest that all of the Type 2 clumps have similar properties with a typical mass and radius of $\sim 10^3 M_{\odot}$ and 0.5 pc, respectively. By contrast, the properties of the other type clumps are widely distributed in the diagrams. Two Type 1 clumps, 3890a and 3890b, have a very large mass of $\sim 4000 M_{\odot}$ and they are lying in a locus similar to that of the Type 2 clumps in Figure 11, suggesting that they are potential sites of cluster formation in the future. However, as we will show in Section 4.1, the Type 1 clumps exhibit puzzling chemical compositions. We will discuss the origin of the Type 1 clumps in Section 4.3.

4. DISCUSSION

At a glance, we would expect that the clump + cluster systems should evolve from Type 1 to Type 4 successively, but this needs a careful inspection of the obtained data set. In the following, we will examine the chemical compositions of the clumps which can be used as a measure of their ages in terms of chemical reaction. We will then inspect the velocity structures as well, and will discuss how the the clump + cluster systems should evolve.

4.1. Chemical Compositions of the Clumps

Up to date, the CCS emission has been detected mostly toward dense regions in low-mass star forming regions, but not in active cluster forming regions such as DR21, W3, or W40 (e.g., Lai & Crutcher 2000; Shimoikura et al. 2015). In this study, we detected the CCS emission for the first time in active cluster forming clumps, i.e., toward the three Type 2 clumps 4753a, 4753b, and 4974. The CCS emission was also detected in one non-cluster forming Type 1 clump (3890a), which was already reported by Sakai et al. (2006).

The relationships between the clumps and the IR clusters suggest that the clumps classified as Types 1 – 3 are in different stages of evolution. To investigate this in terms of chemical reactions, we compared $f(\text{CCS})$ and $f(\text{HC}_3\text{N})$ for the nine clumps in which HC_3N was detected. The relation is shown in Figure 13. As explained in Section 3.1, we estimated the upper and lower lim-

its of the fractional abundances for different assumption of T_{ex} . We plotted their geometrical mean values with error bars representing the two limits. In the figure, we also show results of calculations based on a chemical model by Suzuki et al. (1992). They carried out single-dish survey observations toward 49 dark cloud cores in low-mass star forming regions, and also performed the model calculations to find that CCS and HC_3N are more abundant in an early stage of chemical evolution. Their results were also confirmed by Hirota et al. (2009). The fractional abundances of CCS and HC_3N can therefore be regarded as a good measure of chemical reaction time in dense cores just before/after the formation of stars therein.

In Figure 13, we also show the $f(\text{CCS})$ and $f(\text{HC}_3\text{N})$ data points for dark cloud cores for comparison, which we reported earlier (Shimoikura et al. 2012). We note that the plots for the Types 2 and Type 3 clumps in the figure are likely to be shifted from the global trend of the dark cloud cores, though the ambiguity is large. Although we do not understand clearly the reason for the shift at the moment, it may reflect a significant difference in chemical reactions in massive clumps with IR clusters and small dark cloud cores.

To better establish the evolutionary stages of the Type 1–3 clumps, we compared in Figure 14 $\bar{f}(\text{CS})$ the average fractional abundance of CS and $\bar{f}(\text{SO})$ that of SO within the clump surface S for the 24 clumps. We also plot the same relation for the clumps in our earlier paper (Shimoikura et al. 2013). It is also known that CS and SO can be used as a chemical clock (e.g., Bergin & Langer 1997), and it is expected that CS should appear in an early stages of chemical reactions in molecular clumps, while SO should appear in a later stage. We also show a theoretical model calculated by Bergin & Langer (1997) in the figure. According to the calculations based on their “model 1”, $f(\text{CS})$ and $f(\text{SO})$ start to decrease monotonically at $\sim 2 \times 10^5$ yr and $\sim 2 \times 10^6$ yr, respectively.

As seen in Figure 14, the distribution of the clumps can be well separated according to their types. The figure shows that $\bar{f}(\text{CS})$ and $\bar{f}(\text{SO})$ are decreasing in the order of Type 2, Type 3, and Type 1. In general, difference in the chemical composition can be caused not only by the ages but also by the density of the clumps. However, the latter may not be an important cause for the clumps studied here, because most of them have similar densities in the range $10^4 - 10^5 \text{ cm}^{-3}$ (Figure 11).

We further compared the $f(\text{CCS})$ vs. $f(\text{HC}_3\text{N})$ and $\bar{f}(\text{CS})$ vs. $\bar{f}(\text{SO})$ relations with known cluster ages. The ages of the clusters associated with the clumps 4753a and 4753b are estimated to be ~ 3 Myr (for NGC2264, e.g., Sung et al. 2004) and those of clump 4974 is esti-

mated to be $\sim 1 - 4$ Myr (for Mon R2, e.g., [Maaskant et al. 2011](#)). As seen in Figure 13 and 14, it is interesting to note that the ages of the clusters associated with the Type 2 clumps ($\sim 1 - 4$ Myr) are consistent with the model calculations by [Suzuki et al. \(1992\)](#) and [Bergin & Langer \(1997\)](#). However, we should note that the models assume the gas temperature of only 10 K for dark clouds and do not take into account the feedback of star formation, and thus we cannot directly compare the ages of the clusters with the chemical reaction time of the models. Though it is difficult to take into account the feedback of star formation, recent chemical model calculations for much warmer clumps (up to 200 K, e.g., [Chapman et al. 2009](#); [Hassel et al. 2011](#)) show that fractional abundances of carbon-chain species such as CCS and HC_3N generally decrease in the time range roughly from $\sim 1 \times 10^5$ yr to $\sim 1 \times 10^6$ yr in the same way as for cold dark clouds (10 K) but with shorter reaction time for higher gas temperatures. Because the observed clumps are warmer in the order of the Type 2, Type 3, and Type 1 clumps (see Tables 3 and 4), the loci of the Types 1–3 clumps in Figures 13 and 14 indicate that the Type 2 clumps are the youngest and the Type 1 clumps are the oldest among the three types in terms of chemical compositions.

In summary, the differences in the fractional abundances of CCS, HC_3N , CS, and SO among the three types of the clumps are likely to reflect the different evolutionary stages of the clump types: The Type 1 clumps are seen in the lower-left side of the diagram in Figure 14, suggesting that they may be rather old in terms of chemical compositions. The Type 2 clumps are in an early stage of cluster formation, in which the associated clusters are still embedded in an amount of gas and dust. The Type 3 clumps are in a more evolved stage than the Type 2 clumps with much less molecular gas. The Type 4 clusters with no or very little gas should be in the final stage of cluster formation. We suggest that the massive clumps should evolve in the order of Type 2, 3, and 4 successively.

The Type 1 clumps are puzzling, because we would expect that they are the clumps just before the onset of cluster formation in a stage prior to the Type 2 clumps, but their chemical compositions indicate that they are older than the Type 2 clumps. We will discuss the nature and origin of the Type 1 clumps in Section 4.3.

4.2. Velocity Structures of the Clumps

The results shown in Figures 11–12 suggest that there are interesting systematic differences among the types of the clumps. In the following, we further investigate the velocity structures of the Types 1–3 clumps.

Figure 15 shows the distribution of the velocity dispersion σ_{obs} measured with the ^{13}CO and C^{18}O emission

lines for the 24 clumps as a function of the projected distance from the cluster center (for Type 2 and Type 3 clumps) or from the clump peak (for Type 1 clumps). Values of σ_{obs} measured with the two emission lines are shown by dots with different colors; gray and pink for the ^{13}CO and C^{18}O emission lines. We found that σ_{obs} at the center of the clumps differs depending on the types of the clumps; the σ_{obs} values of Type 1 (except for clumps 3890a and 3890b), Type 2 (except for 4417b), and Type 3 are mostly $\lesssim 0.5 \text{ km s}^{-1}$, $\gtrsim 1.0 \text{ km s}^{-1}$, and $\gtrsim 0.5 \text{ km s}^{-1}$, respectively. This suggests that the large velocity dispersion at the clump center is a typical feature of cluster-forming Type 2 and Type 3 clumps. The velocity dispersion is especially large in the Type 2 clumps, indicating that there must be a lot of motions around the clump center in the beginning of cluster formation.

We also investigated the C^{18}O distributions based on the position-velocity (PV) diagrams for all of the clumps. In Figure 16, we show examples of the PV diagrams measured along the major and minor axes of the clumps, which are displayed in panels (b) and (c) of the figure. As denoted by the white broken circles in panels (b), we found that the PV diagrams of some Type 2 clumps measured along the major axis show double peaks separated by $\sim 1 \text{ km s}^{-1}$, and they are symmetrically located with respect to the clump centers. This feature is seen only in three of the seven Type 2 clumps (4417c, 4423a, and 4753b), but not in Type 1 or Type 3 clumps.

A possible interpretation for the double-peaked feature of the Type 2 clumps could be a collision of two smaller clumps (e.g., [Higuchi et al. 2009](#)), but in that case, we would expect that the velocity difference of the two peaks should largely vary, because the collision velocity is a free parameter and can take any values basically. However, the velocity differences seen in the PV diagrams for clumps 4417c, 4423a, and 4753b are rather small being always only $\lesssim 1 \text{ km s}^{-1}$, suggesting that the double-peaked feature in the PV diagrams is unlikely to be caused by the clump collisions.

To understand the velocity structure of these Type 2 clumps, we analyzed the C^{18}O data of clump 4423a (S235AB) in our previous paper ([Shimoikura et al. 2016](#)), which shows the double-peaked feature most clearly among the three Type 2 clumps, and concluded that the observed feature around the clump center should be caused by the infalling motion with rotation of the entire clump, not by the collisions of smaller clumps. Note that the double-peaked feature in the PV diagram is very similar to those observed around dense cores forming a single low-mass YSO, which was successfully interpreted by [Ohashi et al. \(1997\)](#) as an infalling core with rotation. As we described in details in the previous

paper (Shimoikura et al. 2016), we made a simple model of a massive cluster forming clump ($\sim 1000M_{\odot}$) with analog to the model suggested by Ohashi et al. (1997) for a small core forming a single YSO (see their Figure 8 and Appendix), and we confirmed that the model can reproduce well the PV diagrams observed toward clump 4423a. Obviously, the other Type 2 clumps shown in Figure 16 (4417c and 4753b) also exhibit the double peaks in the PV diagram, indicating that these clumps should also be infalling, although they are too complex to fit nicely with our simple model. Actually, the collapsing motion of clump 4753b was suggested also by Peretto et al. (2006) who found the two velocity components through molecular line observations using the IRAM 30 m telescope.

The above findings imply that, in the beginning of cluster formation, the massive cluster-forming clumps ($\sim 1000M_{\odot}$) have a simple structure similar to a small dense core forming a single low mass star, and we would expect that the dense massive core and therefore the most massive star(s) in the cluster should form at the center of the clump. Such a scenario is supported by recent numerical simulations (Smith et al. 2009; Wang et al. 2010). In the case of the three Type 2 clumps shown in Figure 16 (4423a, 4417c, 4753b), some observational evidences for the formation of massive cores and YSOs at the clump center can also be found in the literature (Felli et al. 2004; Peretto et al. 2006; Dewangan & Anandarao 2011).

The fact that at least three of the seven Type 2 clumps exhibit the double-peaked feature indicates that the infalling motion with rotation of the entire massive clumps is a common phenomenon in the Type 2 clumps. We note that all of the Type 2 clumps showing the highest $f(\text{CS})$ and $f(\text{SO})$ are the ones exhibiting the double-peaked feature in the PV diagrams, indicating that the dynamical infall with rotation occurs in the beginning of cluster formation.

For the rest of Type 2 clumps (3921, 4417b, 4753a, 4974), the double-peaked feature is not seen in our data set, but it can be due to rather poor angular resolution of the observations ($22''$). In fact, the clumps show large velocity gradient along their major axes similar to those observed toward the three clumps with the double-peaked feature, suggesting that they are collapsing but the double-peaked features are not resolved by the current observations.

4.3. Nature of the Observed Massive Type 1 Clumps and the Possible Evolutionary Scenario of the Cluster Formation

As discussed in Section 4.1, the observed Type 1 clumps are generally older than the Type 2 clumps in terms of chemical compositions. Some of the small Type

1 clumps ($\sim 100 M_{\odot}$) can be remnants of the Type 3 clumps, or they might be too small to produce clusters and have survived for a long time without collapsing for some reasons, e.g., by maintaining turbulence by outflows driven by one or a few low-mass YSOs forming there (Snell 1987; Dobashi et al. 1993; Nakamura & Li 2011), or by the support of the magnetic field like what has been suggested for small clouds in the Ophiuchus north region (Nozawa et al. 1991; Hirota et al. 2009). However, the massive Type 1 clumps, namely 3890a and 3890b with a mass of $\sim 4000 M_{\odot}$ are rather mysterious, because, except for their puzzling chemical compositions, they appear to be the very initial clumps that should evolve to Type 2 clumps in terms of the mass and velocity structures. Here, we focus on the nature of these massive Type 1 clumps.

As indicated in Figure 11, these clumps lie in the same loci as Type 2 clumps in the figures, and they appear to be potential sites of cluster formation in the future. The Type 1 clumps are associated with several Class I sources (Jose et al. 2016), and 3890a is associated with a molecular outflow (in Figure 8), and thus sporadic star formation should be taking place there. However, the clumps are not associated with any apparent clusters nor they don't show the double-peaked features in the PV diagrams, suggesting that they are not collapsing but should be gravitationally stable on the clump-scale. Based on the calculations denoted in Section 3.6, we found that the turbulence of the Type 1 clumps is not large enough to support the clumps by itself (i.e., $M_{\text{vir}} < M_{\text{LTE}}$), and therefore additional clump-supporting force is needed. An easy solution for the additional force is the magnetic field. The clumps would be gravitationally stable if they are supported by rather strong magnetic field of an order of ~ 1 mG. In other words, the clumps may be magnetically subcritical (Nakano 1985; Shu et al. 1987), i.e., their collapsing motions by the self-gravity are prevented by the magnetic field. Observational data compiled by Crutcher et al. (2010) show that the magnetic field of this strength (~ 1 mG) is possible at the density of the clumps ($\sim 10^5 \text{ cm}^{-3}$). We therefore suggest that the massive Type 1 clumps (3890a and 3890b) have been stable for a long time due to the strong magnetic field, which may be the reason why they are chemically older than the Type 2 clumps. The clumps have a potential to collapse and evolve into the Type 2 clumps in the future, whenever the support by the magnetic field is weakened.

Type 2 clumps such as 4423a and 4753b forming clusters must have evolved from Type 1 clumps which used to be younger in terms of chemical compositions being located in earlier stages in Figures 13 and 14 than the observed Type 2 clumps. It is likely that such Type 1

clumps are not found in our sample. The reason why we don't find them in our sample is probably their short lifetime. The Type 1 clumps have a typical density of $\sim 1 \times 10^5 \text{ cm}^{-3}$ (Figure 11) corresponding to the free-fall time of only $\tau_{ff} \simeq 10^5 \text{ yr}$, and thus they should contract as soon as they lose the internal supporting forces such as the turbulence and the magnetic field. Beside the Type 1 clumps, ages of the clusters forming in the Type 2 clumps are $> 1 \times 10^6 \text{ yr}$, and therefore the probability to find such Type 1 clumps should be less than 1/10 of that for the Type 2 clumps. This should be the reason why it is difficult to find such Type 1 clumps.

All of the above imply how the clumps of different types should evolve: When massive and dense Type 1 clumps ($\sim 1000 M_\odot$, $\sim 10^5 \text{ cm}^{-3}$) are formed, they are initially stable being supported by the turbulence and magnetic field. They start collapsing and evolve into Type 2 clumps as soon as they lose the clump-supporting forces, or they remain as Type 1 clumps without collapsing if they maintain the clump supporting forces (e.g., the magnetic field of an order of $\sim 1 \text{ mG}$). The Type 2 clumps collapse on the clump-scale, and form clusters at the clump center. Along with the growth of the clusters, the clumps disperse by the feedback of cluster formation (e.g., powerful outflows and stellar wind), which corresponds to our Type 3 category. At the end, only clusters remain (Type 4). In Figure 17, we schematically summarize the above evolutionary scenario of the cluster-forming clumps.

5. CONCLUSIONS

To study cluster formation processes systematically, we carried out observations of 15 dust condensations selected from a catalog compiled by Dobashi (2011) in various molecular lines using the NRO 45 m telescope. The main results of the observations can be summarized as follows:

1. The observations resolved the 15 dust condensations into 24 molecular clumps in the C^{18}O data whose masses vary from 5 to $4397 M_\odot$. We also analyzed the 2MASS point source catalog to investigate the star density distributions of the associated clusters, and identified 23 clusters in the observed regions. Among the 24 clumps, 16 are associated with one or more IR clusters, whereas the other eight are not associated with apparent IR clusters. We also detected nine outflow sources in the 24 clumps, and two of the outflows are newly identified by this study.
2. To assess the relationship between the clumps and IR clusters, we investigated the spatial correlations between $N(\text{H}_2)$ and the star densities, and classified the clumps and IR clusters into four types:

eight clumps having no associated IR clusters are classified to Type 1, seven clumps showing good correlations with IR clusters are classified to Type 2, nine clumps showing poor correlations with IR clusters are classified to Type 3, and six IR clusters with no associated clumps are classified to Type 4.

3. The Type 2 clumps have a typical mass of $\sim 1 \times 10^3 M_\odot$, a radius of $\sim 0.5 \text{ pc}$, and a density of $\sim 1 \times 10^5 \text{ cm}^{-3}$, and the distributions of the associated clusters coincide well with the C^{18}O distributions, indicating that the clusters are forming around the center of the clumps. The velocity dispersion in the Type 2 clumps tends to be larger ($> 0.5 \text{ km s}^{-1}$) at the cluster center. We found that such Type 2 clumps are accompanied by two velocity components that differ by $\sim 1 \text{ km s}^{-1}$, which can be recognized as the two peaks in the position-velocity diagram. On the other hand, neither Type 1 nor Type 3 clumps exhibit such velocity structures. In our previous paper, we presented an evidence that the clump 4423a (Type 2) showing the two velocity components is infalling with rotation on the clump-scale. In this paper, we found at least two similar cases (4417c and 4753b) in the other Type 2 clumps, which indicates that the infalling motion with rotation is a common phenomenon among the Type 2 clumps.
4. We suggest that the clump + IR cluster systems should evolve from Type 1 to Type 4. The Type 1 clumps are stable in the beginning and evolve into Type 2 clumps as soon as they lose the clump-supporting forces, and the Type 2 clumps are collapsing on the clump-scale to form clusters at the clump center. The Type 3 clumps are in a more advanced stage with much less molecular gas, and the Type 4 clusters are more evolved and their natal clumps have already dispersed. All of the clumps classified to Type 1 in this study are older than the Type 2 clumps in terms of chemical compositions. We suggest that they are the Type 1 clumps being gravitationally stable without collapsing for a long time due to the strong magnetic field, or that they are the remnants of Type 3 clumps. Type 1 clumps which are younger than the observed Type 2 clumps in terms of chemical composition should be rare to find due to their short lifetime.

This work was financially supported by Grant-in-Aid for Scientific Research (Nos. 17H02863, 17H01118,

26287030, 17K00963) of Japan Society for the Promotion of Science (JSPS). The 45 m radio telescope is operated by NRO, a branch of NAOJ.

REFERENCES

- Asayama, S., & Nakajima, T. 2013, *PASP*, 125, 213
- Bergin, E. A., Alves, J., Huard, T., & Lada, C. J. 2002, *ApJL*, 570, L101
- Bergin, E. A., & Langer, W. D. 1997, *ApJ*, 486, 316
- Bica, E., Dutra, C. M., & Barbuy, B. 2003a, *A&A*, 397, 177
- Bica, E., Dutra, C. M., Soares, J., & Barbuy, B. 2003b, *VizieR Online Data Catalog*, 340, 40223
- Bohlin, R. C., Savage, B. D., & Drake, J. F. 1978, *ApJ*, 224, 132
- Buckle, J. V., Richer, J. S., & Davis, C. J. 2012, *MNRAS*, 423, 1127
- Burns, R. A., Imai, H., Handa, T., et al. 2015, *MNRAS*, 453, 3163
- Camargo, D., Bonatto, C., & Bica, E. 2011, *MNRAS*, 416, 1522
- Cambr  sy, L., Beichman, C. A., Jarrett, T. H., & Cutri, R. M. 2002, *AJ*, 123, 2559
- Cardelli, J. A., Clayton, G. C., & Mathis, J. S. 1989, *ApJ*, 345, 245
- Carpenter, J. M. 2000, *AJ*, 120, 3139
- Carpenter, J. M., Snell, R. L., & Schloerb, F. P. 1990, *ApJ*, 362, 147
- Chapman, J. F., Millar, T. J., Wardle, M., Burton, M. G., & Walsh, A. J. 2009, *MNRAS*, 394, 221
- Chauhan, N., Pandey, A. K., Ogura, K., et al. 2011, *MNRAS*, 415, 1202
- Crutcher, R. M., Wandelt, B., Heiles, C., Falgarone, E., & Troland, T. H. 2010, *ApJ*, 725, 466
- Dewangan, L. K., & Anandarao, B. G. 2011, *MNRAS*, 414, 1526
- Dierickx, M., Jim  nez-Serra, I., Rivilla, V. M., & Zhang, Q. 2015, *ApJ*, 803, 89
- Dobashi, K. 2011, *PASJ*, 63, 1
- Dobashi, K., Bernard, J.-P., Yonekura, Y., & Fukui, Y. 1994, *ApJS*, 95, 419
- Dobashi, K., Marshall, D. J., Shimoikura, T., & Bernard, J.-P. 2013, *PASJ*, 65, 31
- Dobashi, K., Matsumoto, T., Shimoikura, T., et al. 2014, *ApJ*, 797, 58
- Dobashi, K., Onishi, T., Iwata, T., et al. 1993, *AJ*, 105, 1487
- Dzib, S. A., Ortiz-Le  n, G. N., Loinard, L., et al. 2016, *ApJ*, 826, 201
- Felli, M., Massi, F., Navarrini, A., et al. 2004, *A&A*, 420, 553
- Frerking, M. A., Langer, W. D., & Wilson, R. W. 1982, *ApJ*, 262, 590
- Gutermuth, R. A., Megeath, S. T., Myers, P. C., et al. 2009, *ApJS*, 184, 18
- Hassel, G. E., Harada, N., & Herbst, E. 2011, *ApJ*, 743, 182
- Higuchi, A. E., Kurono, Y., Saito, M., & Kawabe, R. 2009, *ApJ*, 705, 468
- Hirahara, Y., Suzuki, H., Yamamoto, S., et al. 1992, *ApJ*, 394, 539
- Hirota, T., Ohishi, M., & Yamamoto, S. 2009, *ApJ*, 699, 585
- Jeli, J., Kim, J. S., Herczeg, G. J., et al. 2016, *ApJ*, 822, 49
- Kamezaki, T., Imura, K., Omodaka, T., et al. 2014, *ApJS*, 211, 18
- Kawamura, A., Mizuno, Y., Minamidani, T., et al. 2009, *ApJS*, 184, 1
- Kerr, F. J., & Lynden-Bell, D. 1986, *MNRAS*, 221, 1023
- King, I. 1962, *AJ*, 67, 471
- Kirsanova, M. S., Sobolev, A. M., Thomasson, M., et al. 2008, *MNRAS*, 388, 729
- Lada, C. J., & Lada, E. A. 2003, *ARA&A*, 41, 57
- Lai, S.-P., & Crutcher, R. M. 2000, *ApJS*, 128, 271
- Lovas, F. J. 1992, *Journal of Physical and Chemical Reference Data*, 21, 181
- Maaskant, K. M., Bik, A., Waters, L. B. F. M., et al. 2011, *A&A*, 531, A27
- Myers, P. C. 1983, *ApJ*, 270, 105
- Myers, P. C., Fuller, G. A., Mathieu, R. D., et al. 1987, *ApJ*, 319, 340
- Nakamura, F., & Li, Z.-Y. 2011, *ApJ*, 740, 36
- . 2014, *ApJ*, 783, 115
- Nakamura, F., Sugitani, K., Tanaka, T., et al. 2014, *ApJL*, 791, L23
- Nakamura, F., Ogawa, H., Yonekura, Y., et al. 2015, *PASJ*, 67, 117
- Nakano, M., & Yoshida, S. 1986, *PASJ*, 38, 531
- Nakano, M., Soejima, T., Chibueze, J. O., et al. 2017, *PASJ*, 69, 16
- Nakano, T. 1985, *PASJ*, 37, 69
- Nozawa, S., Mizuno, A., Teshima, Y., Ogawa, H., & Fukui, Y. 1991, *ApJS*, 77, 647
- Ohashi, N., Hayashi, M., Ho, P. T. P., & Momose, M. 1997, *ApJ*, 475, 211
- Peretto, N., Andr  , P., & Belloche, A. 2006, *A&A*, 445, 979
- Peretto, N., Hennebelle, P., & Andr  , P. 2007, *A&A*, 464, 983
- Ridge, N. A., Wilson, T. L., Megeath, S. T., Allen, L. E., & Myers, P. C. 2003, *AJ*, 126, 286
- Rieke, G. H., & Lebofsky, M. J. 1985, *ApJ*, 288, 618
- Russeil, D. 2003, *A&A*, 397, 133
- Saito, H., Saito, M., Sunada, K., & Yonekura, Y. 2007, *ApJ*, 659, 459
- Sakai, T., Oka, T., & Yamamoto, S. 2006, *ApJ*, 649, 268
- Sawada, T., Ikeda, N., Sunada, K., et al. 2008, *PASJ*, 60, 445
- Shimajiri, Y., Kitamura, Y., Saito, M., et al. 2014, *A&A*, 564, A68
- Shimoikura, T., Dobashi, K., Matsumoto, T., & Nakamura, F. 2016, *ApJ*, 832, 205
- Shimoikura, T., Dobashi, K., Nakamura, F., et al. 2015, *ApJ*, 806, 201
- Shimoikura, T., Dobashi, K., Sakurai, T., et al. 2012, *ApJ*, 745, 195
- Shimoikura, T., Dobashi, K., Saito, H., et al. 2013, *ApJ*, 768, 72
- Shu, F. H., Adams, F. C., & Lizano, S. 1987, *ARA&A*, 25, 23
- Smith, R. J., Longmore, S., & Bonnell, I. 2009, *MNRAS*, 400, 1775
- Snell, R. L. 1987, in *IAU Symposium*, Vol. 115, *Star Forming Regions*, ed. M. Peimbert & J. Jugaku, 213–236
- Snell, R. L., Huang, Y.-L., Dickman, R. L., & Claussen, M. J. 1988, *ApJ*, 325, 853
- Sung, H., Bessell, M. S., & Chun, M.-Y. 2004, *AJ*, 128, 1684
- Suzuki, H., Yamamoto, S., Ohishi, M., et al. 1992, *ApJ*, 392, 551
- Tiemann, E. 1974, *J. Phys. Chem. Ref. Data*, 3
- Wainscoat, R. J., Cohen, M., Volk, K., Walker, H. J., & Schwartz, D. E. 1992, *ApJS*, 83, 111
- Wang, P., Li, Z.-Y., Abel, T., & Nakamura, F. 2010, *ApJ*, 709, 27
- Wouterloot, J. G. A., & Brand, J. 1989, *A&AS*, 80, 149
- Wouterloot, J. G. A., Brand, J., Burton, W. B., & Kwee, K. K. 1990, *A&A*, 230, 21
- Wright, E. L., Eisenhardt, P. R. M., Mainzer, A. K., et al. 2010, *AJ*, 140, 1868
- Wu, Y., Wei, Y., Zhao, M., et al. 2004, *A&A*, 426, 503
- Xu, Y., Reid, M. J., Zheng, X. W., & Menten, K. M. 2006, *Science*, 311, 54
- Yamamoto, S., Saito, S., Kawaguchi, K., et al. 1990, *ApJ*, 361, 318

Table 1. List of Observed Dust Condensations

Dust Condensation No. ⁽¹⁾	IR cluster ^a	Associated Objects	Distance (kpc)
3645	Y	S172	2.4 ⁽²⁾
3890	Y	S190, AFGL333, IC1805-W, BRC5	2.0 ⁽³⁾
3921	Y	S199, AFGL4029	2.1 ⁽⁴⁾
3923	Y	S201	2.1 ⁽⁴⁾
3935	0.9 (For S202 ⁽²⁾)
3937	0.9 (For S202 ⁽²⁾)
4054	Y	BFS32	0.6 ⁽²⁾
4059	0.6 (For BFS52 ⁽²⁾)
4398	0.81 ^b
4417	Y	S235	1.56 ⁽⁵⁾
4423	Y	S235A, B	1.56 ⁽⁵⁾
4565	Y	BFS51	1.6 ⁽⁶⁾
4678	1.0(For S268 ⁽²⁾)
4753	Y	Mon OB1-D, NGC2264C, D	0.738 ⁽⁷⁾
4974	Y	Mon R2	0.893 ⁽⁸⁾

^a See Table 8 for the references of the IR clusters.

^b For No.4398, we calculated the kinematic distance using the ¹³CO peak velocity obtained with the 45 m observations ($V_{\text{LSR}} = -2.2 \text{ km s}^{-1}$). The distance is calculated using the Galactic rotation model of [Kerr & Lynden-Bell \(1986\)](#), [Wouterloot & Brand \(1989\)](#), and [Wouterloot et al. \(1990\)](#), assuming the distance of the Sun from Galactic Center $R_0 = 8.5 \text{ kpc}$ and the rotation speed of the Galaxy $\Theta_0 = 220 \text{ km s}^{-1}$ at R_0 .

References—⁽¹⁾ [Dobashi \(2011\)](#) ⁽²⁾ [Russeil \(2003\)](#) ⁽³⁾ [Xu et al. \(2006\)](#) ⁽⁴⁾ [Chauhan et al. \(2011\)](#) ⁽⁵⁾ [Burns et al. \(2015\)](#) ⁽⁶⁾ [Carpenter et al. \(1990\)](#) ⁽⁷⁾ [Kamezaki et al. \(2014\)](#) ⁽⁸⁾ [Dzib et al. \(2016\)](#)

Table 2. NRO 45m Observations

Molecule	Transition	Frequency (GHz)	Beam (arcsec)	ΔT_{mb} (K)
CCS	$J_N=4_3-3_2$	45.379033	36''8	0.1 – 0.3
HC ₃ N	$J = 5 - 4$	45.490316	36''7	0.1 – 0.3
C ³⁴ S	$J = 2 - 1$	96.412950	17''3	0.3 – 0.6
CS	$J = 2 - 1$	97.980953	17''0	0.4 – 0.7
SO	$J_N=2_3-1_2$	99.299905	16''8	0.3 – 0.6
C ¹⁸ O	$J = 1 - 0$	109.782176	15''2	0.4 – 0.8
¹³ CO	$J = 1 - 0$	110.201354	15''1	0.5 – 0.9
¹² CO	$J = 1 - 0$	115.271202	14''5	1.2 – 1.8

NOTE—The rest frequency for the CCS line is taken from [Yamamoto et al. \(1990\)](#), and those of the other lines are taken from the website of [Lovas \(1992\)](#).

Table 3. Physical Properties of the Clumps

Clump	$\alpha(\text{J2000})^{\text{a}}$ (^h ^m ^s)	$\delta(\text{J2000})^{\text{a}}$ ([°] ['] ^{''})	R (pc)	$\overline{\Delta V}(\text{C}^{18}\text{O})^{\text{b}}$ (km s ⁻¹)	$\overline{T_{\text{ex}}}^{\text{b}}$ (K)	M_{LTE} (M_{\odot})	M_{vir} (M_{\odot})	$n(\text{H}_2)^{\text{b}}$ (10 ⁴ cm ⁻³)	$\overline{N}(\text{H}_2)^{\text{b}}$ (10 ²² cm ⁻²)	$\overline{N}(\text{C}^{18}\text{O})^{\text{b}}$ (10 ¹⁵ cm ⁻²)	$\overline{f}(\text{SO})^{\text{b}}$ (10 ⁻⁹)	$\overline{f}(\text{CS})^{\text{b}}$ (10 ⁻⁹)	$\overline{f}(\text{C}^{34}\text{S})^{\text{b}}$ (10 ⁻¹⁰)
3645a	00:15:25.0	61:13:17	0.43	2.7	35.8	398	681	1.7	3.9	6.3	1.7	0.9	<1.1
3645b	00:15:29.2	61:14:02	0.41	1.9	38.4	474	347	2.4	3.6	5.8	1.8	1.5	1.7
3890a	02:28:03.1	61:27:39	0.61	2.1	36.0	3432	573	5.2	13.5	23.6	1.7	0.5	2.8
3890b	02:28:04.1	61:29:16	0.62	2.4	35.6	4397	721	6.4	17.3	30.4	1.1	0.3	2.2
3890c	02:28:57.7	61:33:01	0.23	1.1	35.9	113	56	3.2	3.0	4.7	3.3	1.4	<2.0
3921	03:01:30.4	60:29:11	0.57	1.9	50.5	1508	439	2.8	6.7	11.4	1.8	1.8	2.0
3923	03:03:22.5	60:28:03	0.28	1.6	43.0	249	141	3.9	4.6	7.7	2.4	1.2	<0.6
3935	03:15:41.4	60:02:23	0.19	0.9	28.8	25	35	1.2	2.7	4.2	1.3	0.3	<0.3
3937	03:20:38.9	60:17:54	0.21	0.9	26.4	86	32	3.2	2.8	4.4	1.0	0.4	<0.6
4054	03:51:42.7	51:27:52	0.16	1.0	34.9	48	31	4.0	2.7	4.1	1.1	0.4	<0.4
4059	03:56:50.4	51:47:19	0.20	1.3	24.5	71	67	3.1	2.5	3.9	1.7	0.5	<0.8
4398	05:14:09.6	32:45:07	0.10	0.9	34.2	5	14	1.6	1.0	1.2	<0.9	<0.1	<0.9
4417a	05:40:59.7	35:49:20	0.64	3.1	54.4	1852	1464	2.4	6.5	11.1	2.8	1.4	1.3
4417b	05:41:26.9	35:52:12	0.46	1.5	54.8	994	253	3.5	7.6	13.1	2.7	1.1	<0.7
4417c	05:41:29.3	35:48:57	0.40	2.5	56.5	993	609	5.4	8.7	15.0	3.6	1.7	1.7
4423a	05:40:52.9	35:41:35	0.41	2.5	47.7	955	617	4.8	7.9	13.5	4.0	2.9	4.3
4423b	05:40:53.5	35:38:28	0.25	1.5	55.7	177	142	3.9	4.2	6.8	<1.1	<0.8	<1.2
4565a	06:18:36.7	23:18:32	0.19	1.7	58.1	131	115	6.6	5.3	8.8	3.3	1.5	<1.2
4565b	06:18:42.7	23:20:02	0.31	1.6	38.9	331	172	3.8	5.1	8.5	2.1	0.8	<1.0
4565c	06:18:46.0	23:21:17	0.22	1.4	32.9	161	92	5.2	3.7	6.0	2.1	0.7	<0.8
4678	06:09:52.5	13:44:48	0.14	1.4	36.7	26	59	3.3	2.1	3.1	2.0	0.3	<0.9
4753a	06:41:05.0	09:35:15	0.27	2.9	50.6	1123	486	19.8	20.6	36.5	2.1	1.0	1.2
4753b	06:41:10.6	09:29:38	0.35	3.3	50.8	1203	810	9.7	13.6	23.8	4.0	2.0	2.1
4974	06:07:44.4	-06:23:26	0.50	3.3	59.4	2581	1076	7.2	13.3	23.3	1.2	2.2	1.7

^a Peak position of the C¹⁸O ($J = 1 - 0$) integrated intensity in the equatorial coordinates.^b The average value of the clumps.NOTE—For the fractional abundance of SO, we calculated the mean partition function Q to be 76.3 – 176.9 for the assumed T_{ex} of 24.5 – 82.1 K using the parameters measured by [Tiemann \(1974\)](#).

Table 4. Physical Properties Derived from CCS and HC₃N

Clump	α (J2000) (^h ^m ^s)	δ (J2000) ([°] ['] ^{''})	T_{ex}^{a} (K)	$N(\text{H}_2)$ (10^{22}cm^{-2})	$N(\text{CCS})^{\text{b}}$ (10^{12}cm^{-2})	$N(\text{HC}_3\text{N})^{\text{b}}$ (10^{12}cm^{-2})	$f(\text{CCS})^{\text{b}}$ (10^{-10})	$f(\text{HC}_3\text{N})^{\text{b}}$ (10^{-10})
3645a	00:15:30.1	61:14:30	35.9	2.1	$< 1.4 - < 4.9$	$4.7 - 6.5$	$< 0.7 - < 2.3$	$2.2 - 3.1$
3890a	02:28:4.9	61:27:45	36.2	15.6	$8.6 - 29.7$	$8.5 - 11.7$	$0.5 - 1.9$	$0.5 - 0.7$
3890b	02:28:7.0	61:29:15	34.2	19.1	$< 3.0 - < 6.4$	$6.9 - 9.5$	$< 0.2 - 0.3$	$0.4 - 0.5$
3921	03:01:30.0	60:29:15	52.1	6.9	$< 1.7 - < 9.4$	$11.5 - 21.2$	$< 0.2 - 1.4$	$1.7 - 3.1$
4423a	05:40:53.0	35:41:35	47.8	8.9	$< 4.5 - < 5.4$	$16.1 - 27.9$	$< 0.5 - 0.6$	$1.8 - 3.1$
4565b	06:18:43.3	23:19:45	37.4	4.0	$< 2.6 - < 9.2$	$6.0 - 8.5$	$< 0.7 - < 2.3$	$1.5 - 2.1$
4753a	06:40:58.4	09:36:8	50.2	13.4	$10.1 - 46.5$	$30.2 - 53.9$	$0.8 - 3.5$	$2.2 - 4.0$
4753b	06:41:10.6	09:29:23	55.3	18.2	$10.3 - 50.9$	$38.8 - 75.1$	$0.6 - 2.8$	$2.1 - 4.1$
4974	06:07:39.0	-06:22:60	66.1	14.2	$10.1 - 57.6$	$38.6 - 87.4$	$0.7 - 4.1$	$2.7 - 6.2$

NOTE—The parameters were derived at the peak position of the HC₃N integrated intensity. To estimate the column densities of CCS, we calculated Q to be $24.302 - 651.75970$ for the assumed T_{ex} of $5.0 - 66.1$ K using the parameters measured by Yamamoto et al. (1990).

^a T_{ex} calculated using the ¹²CO data.

^b Minimum and maximum estimates for parameters assuming a flat T_{ex} of 5 K and that calculated using the ¹²CO data, respectively.

Table 5. Derived Velocity Dispersion

Clump	$\sigma_{\text{obs}(\text{C}^{18}\text{O})}$ (km s^{-1})	σ_{therm} (km s^{-1})	$\sigma_{3\text{D}}$ (km s^{-1})
3645a	1.16	0.10	1.96
3645b	0.77	0.10	1.32
3890a	0.91	0.10	1.55
3890b	0.82	0.10	1.42
3890c	0.48	0.10	0.84
3921	0.78	0.12	1.33
3923	0.66	0.11	1.14
3935	0.36	0.09	0.60
3937	0.36	0.09	0.60
4054	0.31	0.09	0.51
4059	0.59	0.08	1.00
4398	0.27	0.10	0.44
4417a	0.87	0.12	1.49
4417b	0.70	0.12	1.10
4417c	0.86	0.12	1.53
4423a	1.02	0.11	1.75
4423b	0.62	0.12	1.06
4565a	0.63	0.13	1.07
4565b	0.61	0.10	1.04
4565c	0.59	0.10	1.00
4678	0.45	0.10	0.81
4753a	1.19	0.12	2.05
4753b	1.35	0.12	2.33
4974	1.21	0.13	2.07

Table 6. Derived Parameters of the Outflows.

Clump wing	$\overline{T_{\text{ex}}}$	V_{sys}	V_{char}	V_{range}	S_{lobe}	R_{lobe}	$\int \int T_{\text{mb}} dV dS$	t_d	τ_{max}	$M_{\text{lobe}}^{\text{a}}$	$\dot{P}_{\text{lobe}}^{\text{a}}$	$\dot{P}_{\text{lobe}}^{\text{a}}$
	(K)	(kms^{-1})	(kms^{-1})	(kms^{-1})	(arcsec^2)	(pc)	($\text{K km s}^{-1} \text{arcmin}^2$)	(10^4yr)		(M_{\odot})	($M_{\odot} \text{ km s}^{-1}$)	($10^{-4} M_{\odot} \text{ km s}^{-1} \text{yr}^{-1}$)
3890a blue	35.5	-48.5	9.2	(-59, -53.5)	2981	0.30	8.8	3.2	1.7	1.3 - 2.7	13.3 - 27.4	4.5 - 9.4
red	35.3		8.0	(-44, -40)	2756	0.29	7.0	3.5	2.4	1.1 - 2.8	8.8 - 23.3	2.6 - 6.9
3890c blue	29.3	-51.5	5.4	(-59, -53)	4838	0.38	17.8	7.0	1.5	2.5 - 4.8	14.8 - 28.8	2.4 - 4.6
red	30.0		6.2	(-49, -44)	3544	0.33	9.2	5.1	6.7	1.3 - 8.6	7.3 - 48.9	1.3 - 8.7
3921 blue	47.6	-38.1	7.3	(-46, -41)	10744	0.60	33.7	8.0	6.4	7.7 - 49.6	69.9 - 450.2	10.8 - 69.9
red	44.3		6.4	(-36, -30)	33019	1.05	166.6	16.0	9.9	36.4 - 361.1	271.0 - 2685.5	19.7 - 195.0
4417a blue	58.1	-20.3	7.7	(-28, -24)	5738	0.32	20.2	4.1	3.4	3.0 - 10.4	22.5 - 79.2	5.4 - 19.0
4417c blue	55.6		7.0	(-28, -24)	2925	0.23	8.9	3.2	5.6	1.2 - 6.8	7.9 - 44.3	2.3 - 12.7
4423a blue	53.2	-16.9	7.7	(-24, -20)	3319	0.24	15.5	3.1	2.5	2.1 - 5.7	17.3 - 47.8	6.0 - 16.6
4753a blue	44.9	5.3	11.3	(-9, 1)	13219	0.23	81.9	2.0	2.8	2.1 - 6.3	25.0 - 75.5	13.2 - 39.8
4753b blue	53.6	7.9	12.0	(-6, 2)	787	<0.1	3.2	<0.5	3.7	<0.1 - 0.2	0.4 - 1.6	<0.1 - 3.1
red	52.8		11.3	(13, 20)	7031	0.17	53.3	1.5	3.8	1.5 - 6.0	16.5 - 63.8	10.5 - 40.8
4974 blue	65.0	10.4	10.7	(0, 5.5)	24413	0.38	156.6	3.5	8.1	8.1 - 65.5	82.4 - 670.4	22.5 - 183.1
red	55.4		11.6	(16.5, 22)	40894	0.50	377.8	4.2	8.4	16.9 - 141.7	198.1 - 1665.4	48.0 - 403.8

NOTE—^a Minimum and maximum estimates for parameters of the outflows, which are estimated using $\tau = 0$ and $\tau = \tau_{\text{max}}$, respectively (see Appendix B).

Table 7. Physical Properties of the IR Clusters

IR Cluster	α (J2000) (^h ^m ^s)	δ (J2000) ([°] ['] ^{''})	R_* (pc)	N_*	Peak density (stars arcmin ⁻²)	Dmin/Dmaj ^a
3645cl	00:15:29.2	61:14:25	0.64	63	34	0.5
3890cl1	02:28:16.1	61:31:10	0.76	172	47	0.4
3890cl2	02:28:20.7	61:28:27	0.35	48	63	0.8
3890cl3	02:28:30.4	61:27:17	0.30	29	39	0.9
3890cl4	02:28:47.7	61:33:27	0.35	43	43	0.5
3890cl5	02:29:04.1	61:33:24	0.44	69	59	0.7
3921cl1	03:01:19.3	60:29:28	0.49	59	35	0.8
3921cl2	03:01:33.8	60:29:13	0.45	57	49	0.5
3923cl	03:03:15.3	60:27:58	0.40	63	44	0.8
4054cl	03:51:33.3	51:29:59	0.13	18	24	0.6
4417cl1	05:41:06.9	35:49:24	0.28	33	33	0.5
4417cl2	05:41:10.0	35:50:09	0.27	23	23	0.5
4417cl3	05:41:23.9	35:52:09	0.34	27	25	0.6
4417cl4	05:41:30.8	35:49:53	0.40	47	23	0.4
4423cl1	05:40:54.9	35:44:14	0.35	40	27	0.8
4423cl2	05:40:53.1	35:42:14	0.40	135	65	0.6
4423cl3	05:40:55.5	35:40:07	0.43	80	33	0.6
4423cl4	05:40:52.4	35:38:22	0.25	12	21	0.9
4565cl	06:18:38.1	23:19:18	0.47	94	35	0.6
4753cl1	06:41:04.2	09:35:45	0.19	36	22	0.5
4753cl2	06:41:06.7	09:34:07	0.12	15	16	0.7
4753cl3	06:41:09.7	09:29:37	0.13	34	40	0.6
4974cl	06:07:46.0	-06 : 22 : 55	0.28	380	86	0.7

^a Ratio of the minor axis to the major axis of the cluster surface area fitted with the 2D Gaussian function.**Table 8.** Clumps and IR Clusters

Dust Condensation No.	Clump	IR Cluster ^a	Type	Outflow ^a	IRAS ^b	$L(L_\odot)$ ^c
3645	3645a	3645cl ⁽¹⁾	3	N
	3645b	3645cl ⁽¹⁾	3	N	00127+6058	4.0×10^3
3890	3890a	N	1	Y ⁽⁵⁾
	3890b	N	1	N
	...	3890cl1 ⁽¹⁾	4	N
	...	3890cl2 ⁽²⁾	4	N	02245+6115	1.0×10^4
	...	3890cl3 [†]	4	N
	...	3890cl4 [†]	4	N
	3890c	3890cl5 ⁽¹⁾	3	Y ⁽⁶⁾
3921	...	3921cl1 ⁽²⁾	4	N
	3921	3921cl2 ⁽²⁾	2	Y ⁽⁶⁾	02575+6017	1.3×10^4
3923	3923	3923cl ⁽²⁾	3	N	02593+6016	1.7×10^4
3935	3935	N	1	N
3937	3937	N	1	N
4054	4054	4054cl ⁽¹⁾	3	N
4059	4059	N	1	N

Table 8 continued

Table 8 (*continued*)

Dust Condensation No.	Clump	IR Cluster ^a	Type	Outflow ^a	<i>IRAS</i> ^b	$L(L_{\odot})$ ^c
4398	4398	N	1	N
4417	4417a	4417cl1 ⁽²⁾ , cl2 ⁽³⁾	3	Y [†]
	4417b	4417cl3 ⁽⁴⁾	2	N	05379+3550	3.6×10^3
	4417c	4417cl4 ⁽⁴⁾	2	Y [†]	05382+3547	2.0×10^3
4423	...	4423cl1 ⁽¹⁾	4	N
	4423a	4423cl2 ⁽²⁾	2	Y ⁽⁶⁾⁽⁷⁾	05375+3540	1.3×10^4
	...	4423cl3 ⁽¹⁾	4	N
	4423b	4423cl4 ⁽¹⁾	3	N	05375+3536	8.9×10^3
4565	4565a	4565cl ⁽²⁾	3	N	06155+2319A	5.0×10^3
	4565b	4565cl ⁽²⁾	3	N
	4565c	N	1	N
4678	4678	N	1	N
4753	4753a	4753cl1 ⁽²⁾ , cl2 [†]	2	Y ⁽⁶⁾⁽⁸⁾	06382+0939	4.7×10^2
	4753b	4753cl3 ⁽²⁾	2	Y ⁽⁶⁾⁽⁸⁾	06384+0932	2.5×10^3
4974	4974	4974cl ⁽²⁾	2	Y ⁽⁶⁾	06053-0622	4.2×10^4

^a ‘Y’ indicates detection and ‘N’ indicates no detection.

^b Selected *IRAS* point source using the selection criteria proposed by Dobashi et al. (1994).

^c The bolometric luminosity calculated following the method of Myers et al. (1987).

NOTE—[†] The IR clusters or outflows identified by this work.

References—⁽¹⁾ Bica et al. (2003a) ⁽²⁾ Bica et al. (2003b) ⁽³⁾ Camargo et al. (2011) ⁽⁴⁾ Kirsanova et al. (2008)
⁽⁵⁾ Nakano et al. (2017) ⁽⁶⁾ Wu et al. (2004) ⁽⁷⁾ Nakano & Yoshida (1986) ⁽⁸⁾ Buckle et al. (2012)

Table 9. Molecular Constants

Molecule	Transition	S_{ij}	B_0 (GHz)	μ (Debye)	E_u (cm ⁻¹)
CCS	$J_N=4_3-3_2$	3.972	6.477750	2.88000	3.75568
HC ₃ N	$J=5-4$	5.000	4.549059	3.73172	4.55219
C ³⁴ S	$J=2-1$	2.000	24.103540	1.95700	6.19802
CS	$J=2-1$	2.000	24.495560	1.95700	4.90249
SO	$J_N=2_3-1_2$	2.934	21.523556	1.53500	6.41219
C ¹⁸ O	$J=1-0$	1.000	54.891420	0.11049	3.66194
¹³ CO	$J=1-0$	1.000	55.101010	0.11046	3.67592
¹² CO	$J=1-0$	1.000	57.635960	0.11011	3.84503

NOTE—All of the constants are taken from Splatalogue.

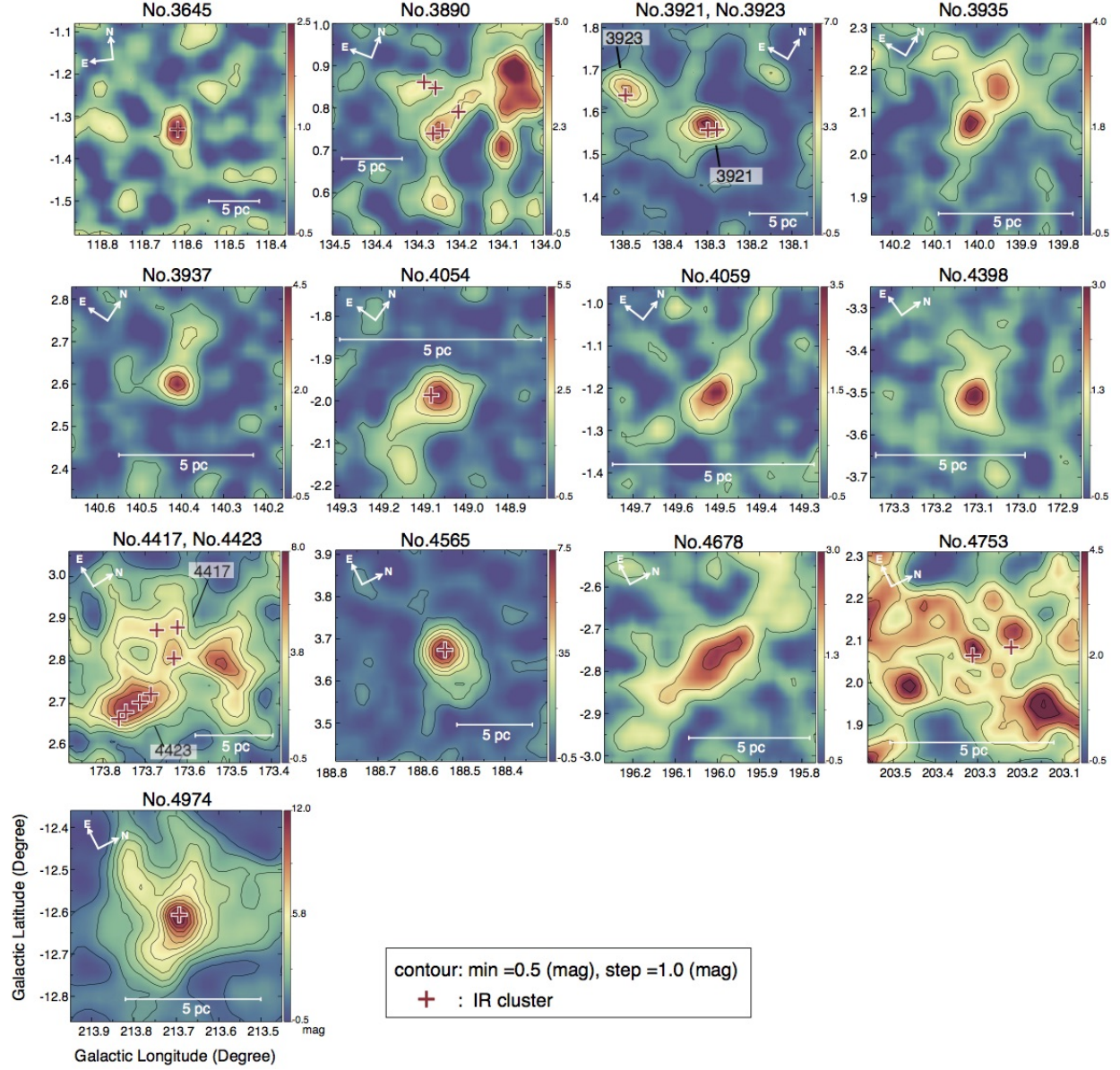


Figure 1. Extinction (A_V) maps of the 15 dust condensations generated by Dobashi (2011) shown in the Galactic coordinates. Contours are drawn from 0.5 mag with an increment of 1.0 mag. Plus signs indicate the positions of the identified IR clusters (See Section 3.4).

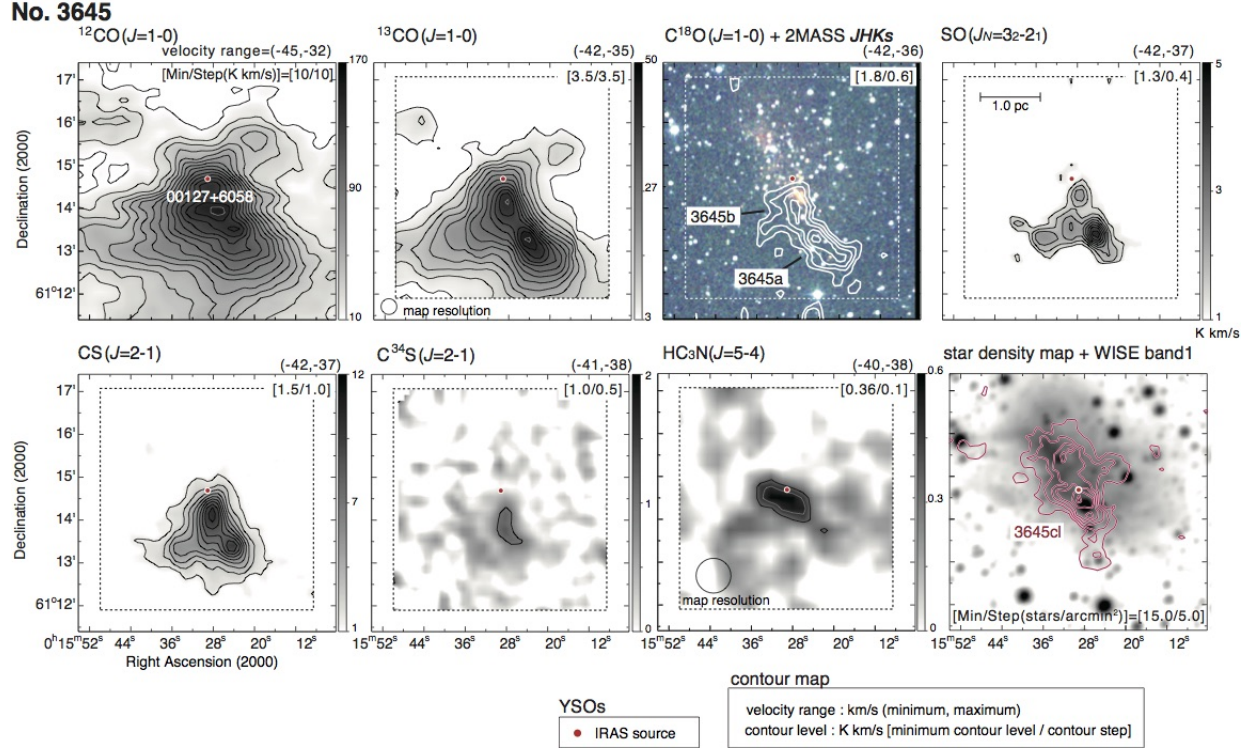


Figure 2. Maps of the integrated intensity of the observed molecular lines around the dust condensation No.3645 obtained with the 45 m telescope, shown in the equatorial coordinates. Molecules, transitions, and the velocity ranges in units of km s^{-1} used for the integration are indicated above the maps. The lowest contours and the contour intervals in units of K km s^{-1} are indicated in the square brackets in each panel. No obvious CCS emission is detected in this dust condensation. The map resolution is indicated by the open circle in panels for the ^{13}CO and HC_3N emission lines. The last panel on the lower right shows the star density map of the cluster 3645cl overlaid with the WISE $3.4 \mu\text{m}$ image (gray scale). The lowest contour and the contour interval in units of arcmin^{-2} are indicated in the panel. The red dot denotes the position of the selected *IRAS* source.

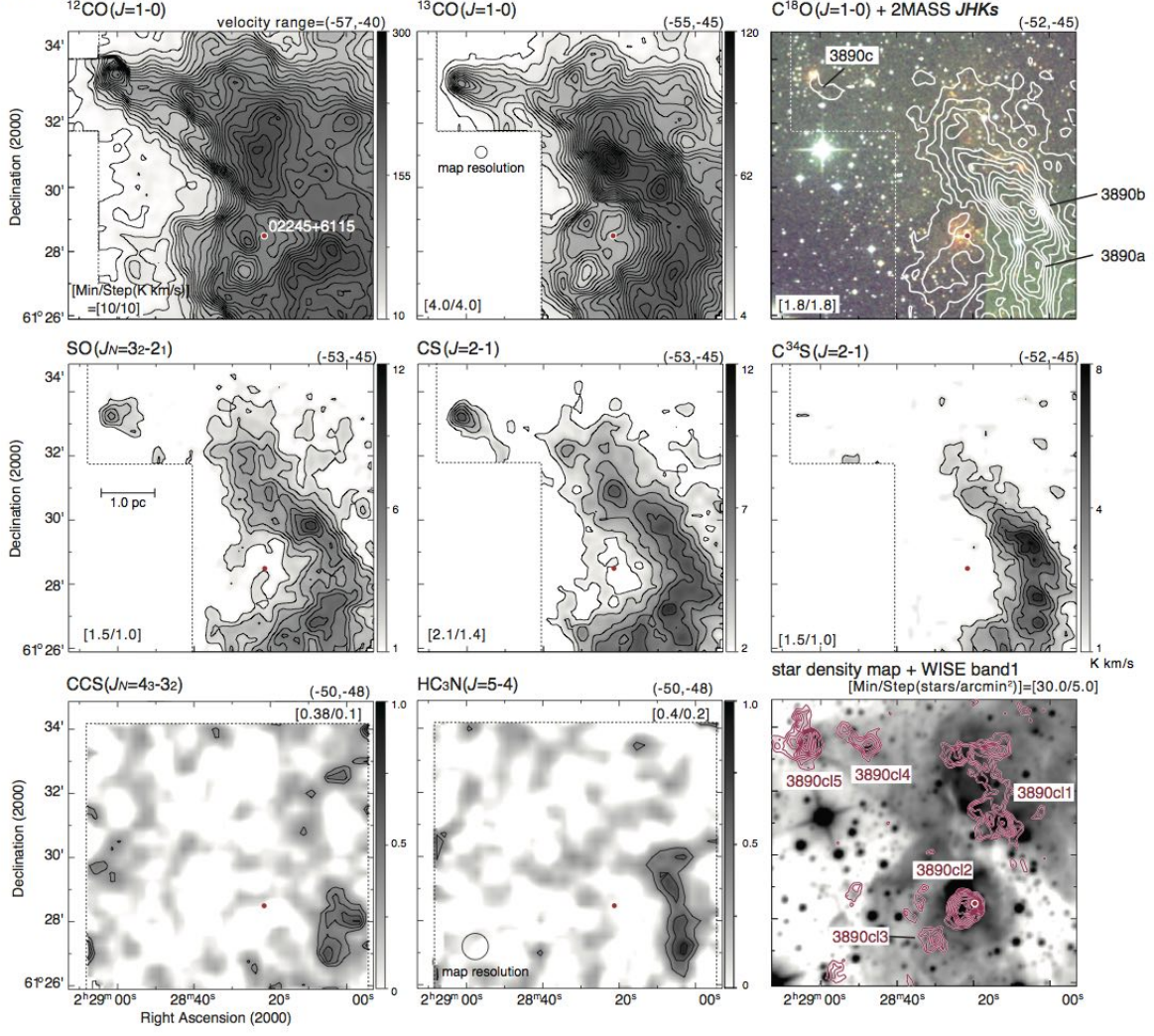
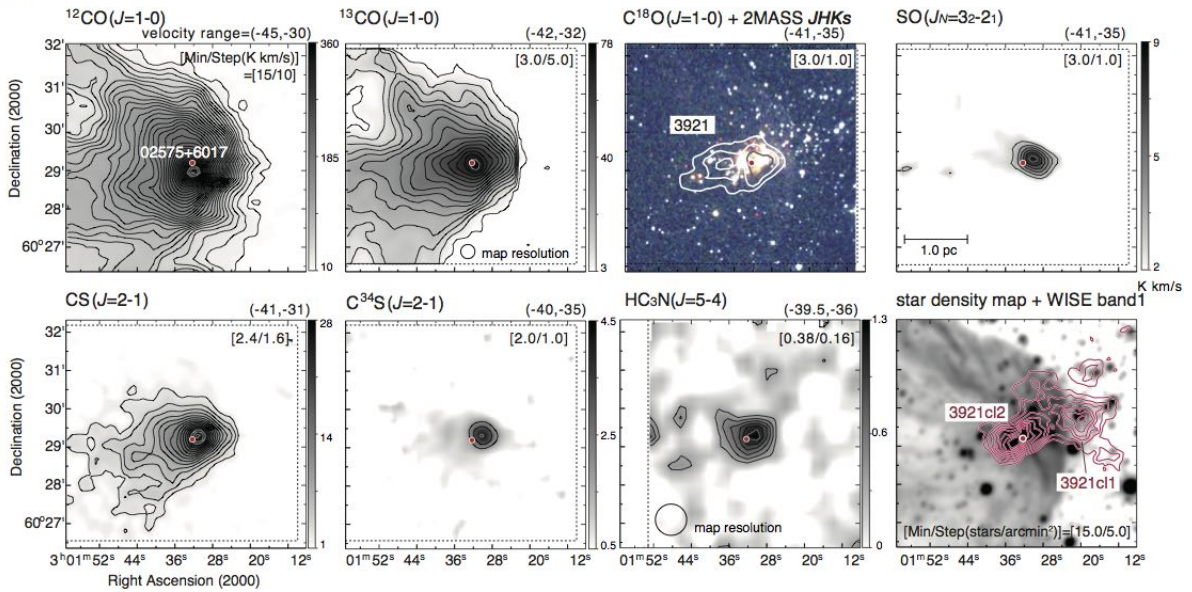
No. 3890**No. 3921**

Figure 3. Same as Figure 2, but for the dust condensations Nos. 3890 and 3921.

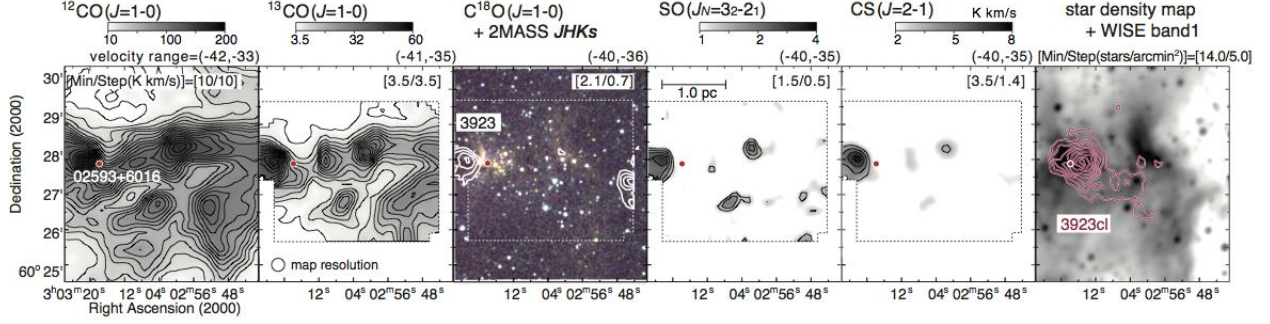
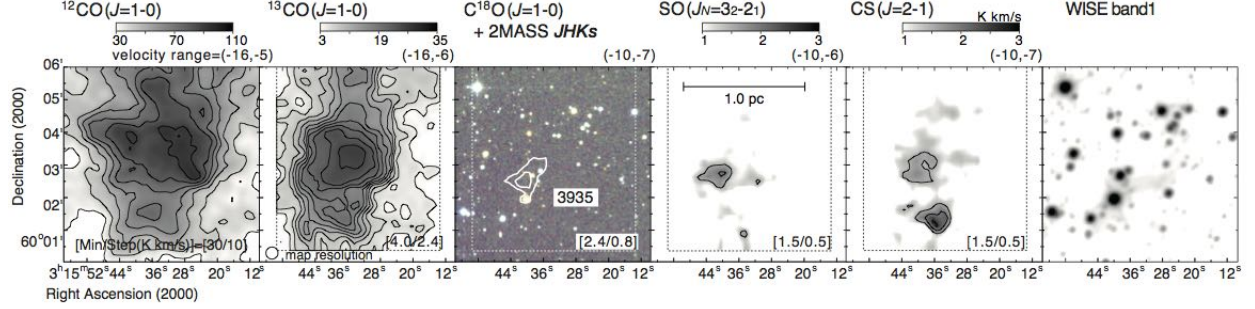
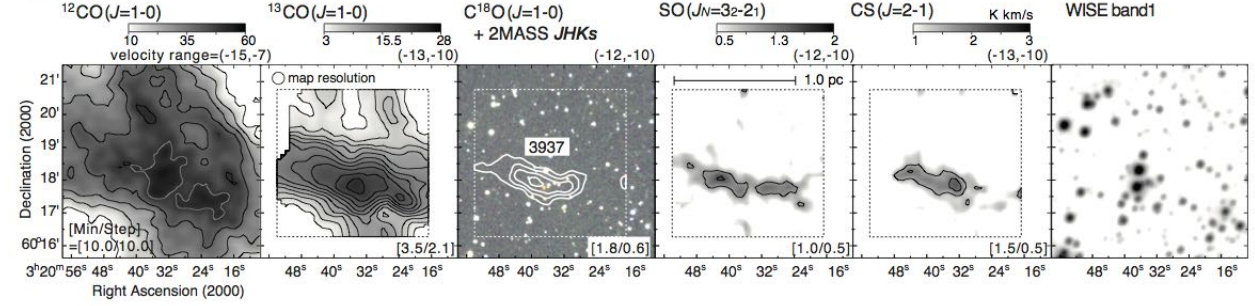
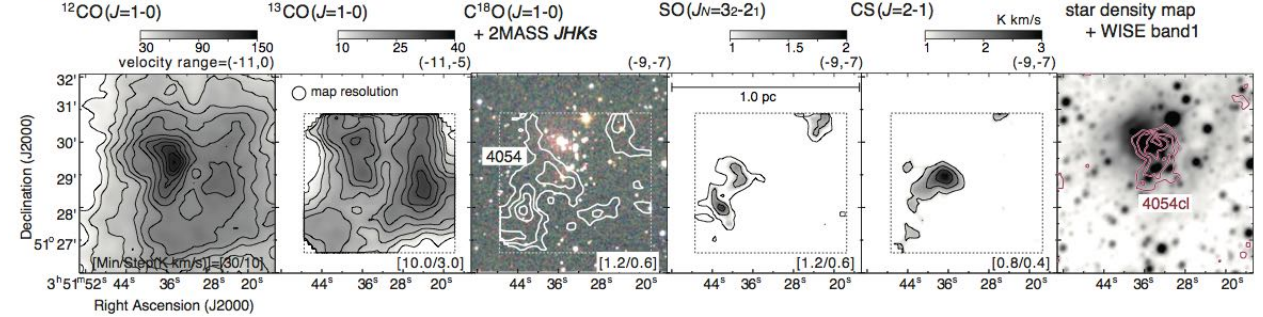
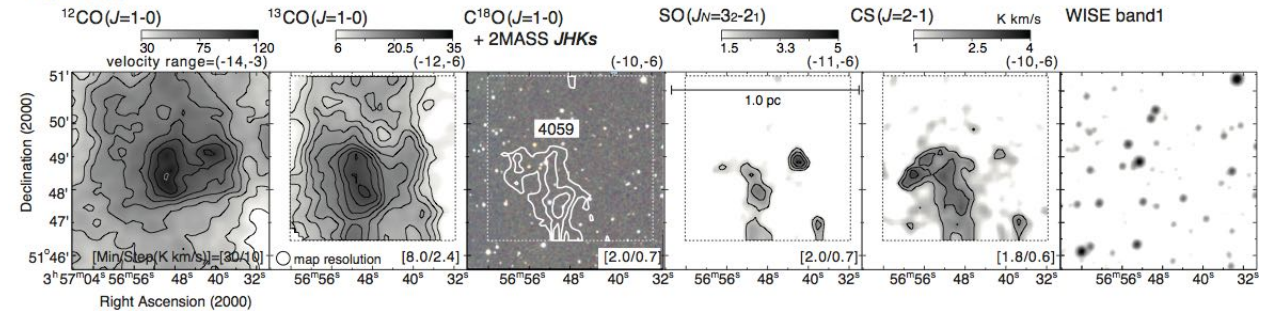
No. 3923**No. 3935****No. 3937****No. 4054****No. 4059**

Figure 4. Same as Figure 2, but for the dust condensations Nos. 3923, 3935, 3937, 4054, and 4059. No obvious C^{34}S emission is detected in all of the dust condensations. No obvious IR cluster is seen in the dust condensations Nos. 3935, 3937, and 4059.

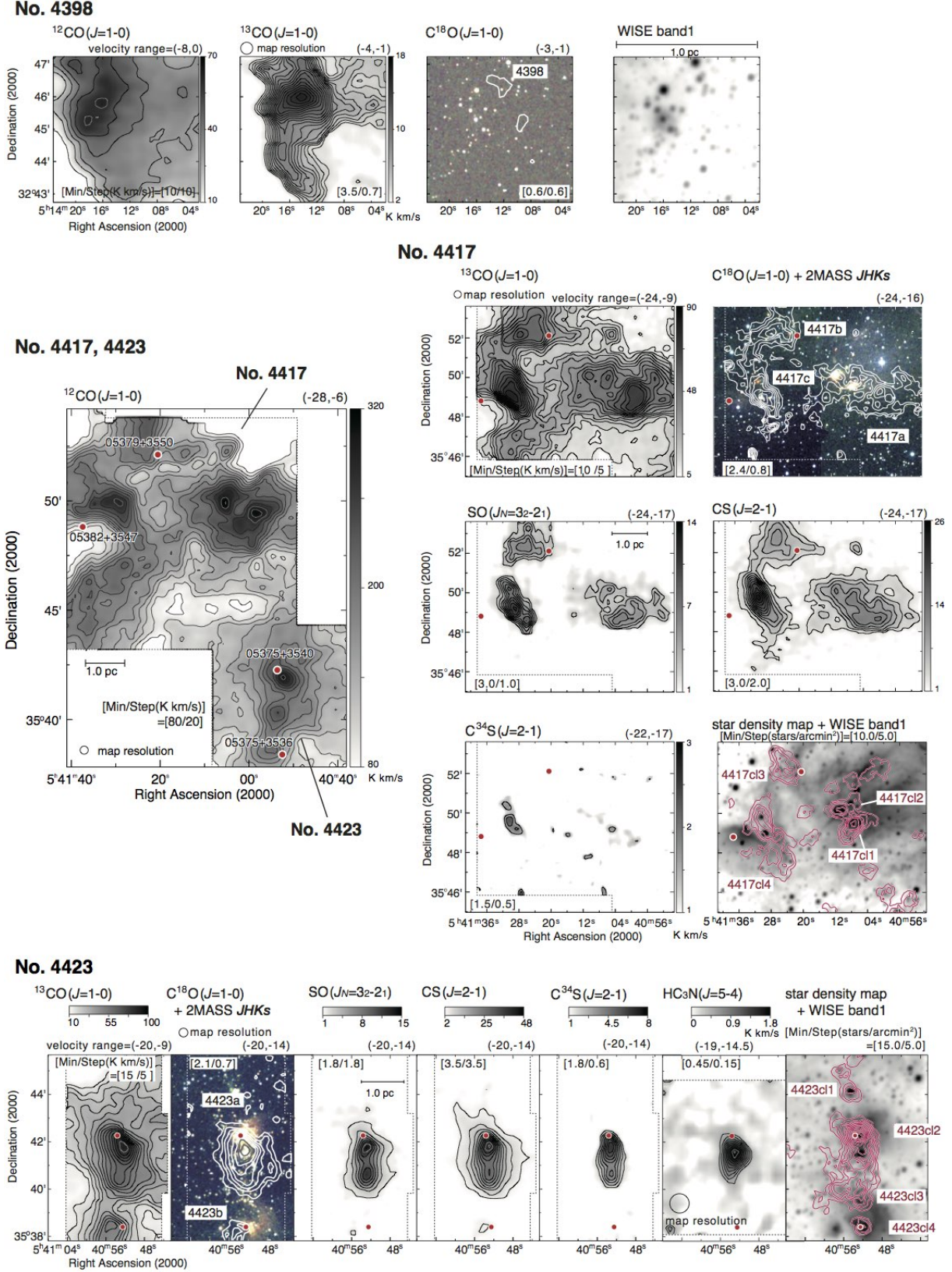


Figure 5. Same as Figure 2, but for the dust condensations Nos. 4398, 4417, and 4423. No obvious SO, CS, $C^{34}S$ emission or IR cluster are seen in the dust condensation No.4398.

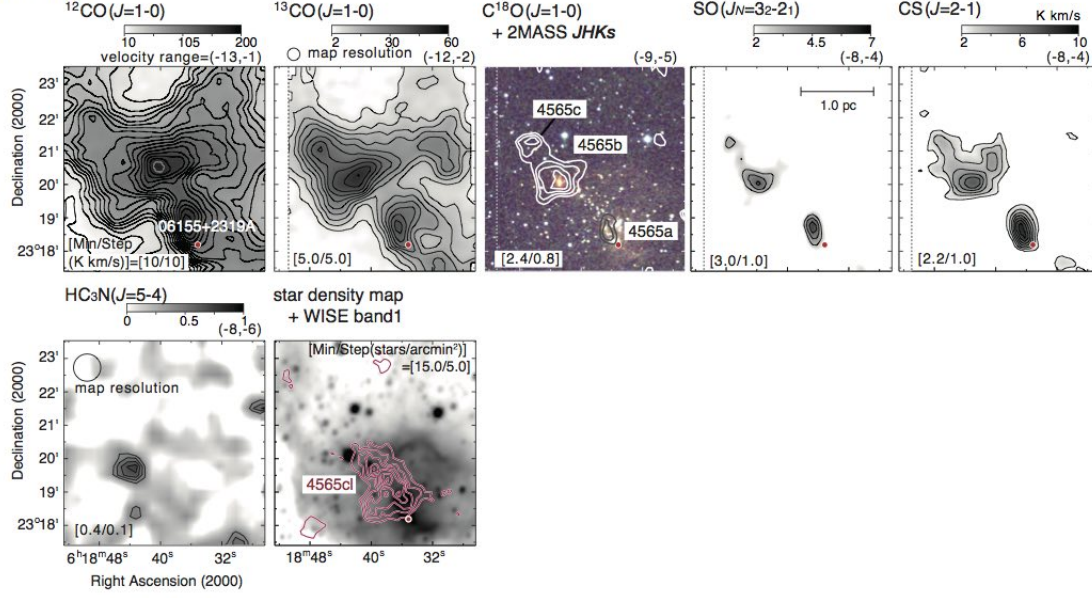
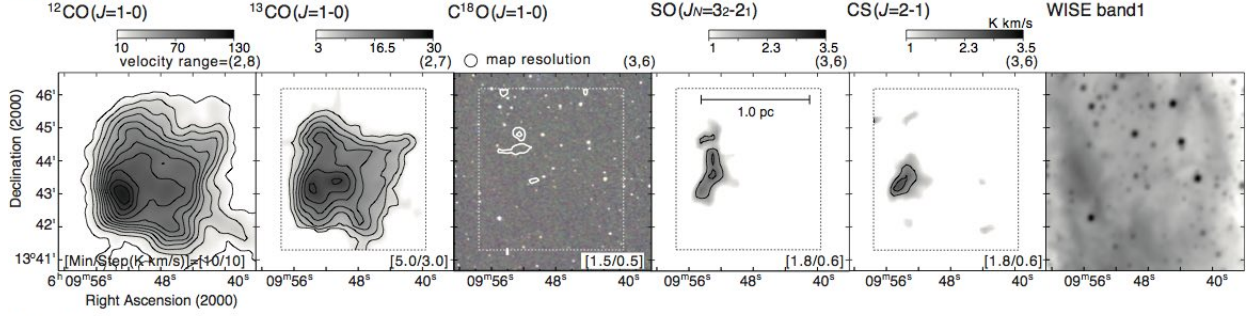
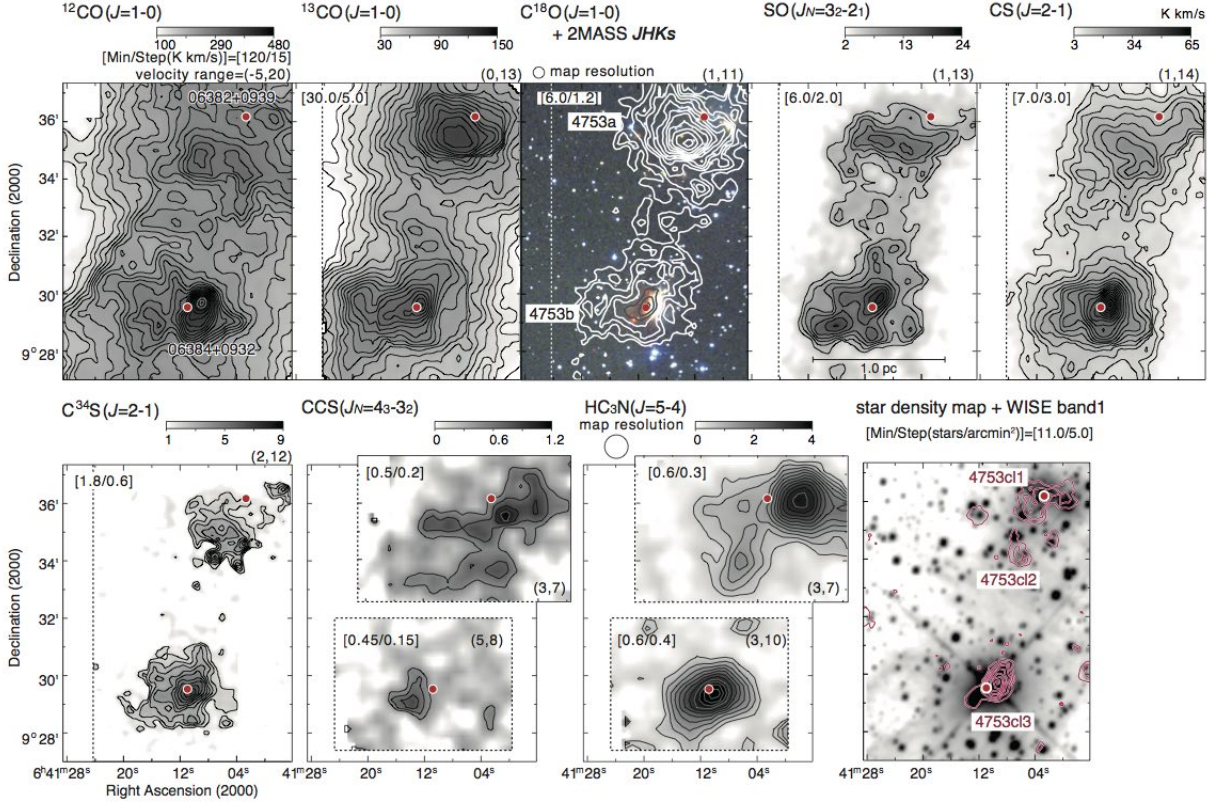
No. 4565**No. 4678****No. 4753**

Figure 6. Same as Figure 2, but for the dust condensations Nos. 4565, 4678, and 4753. No obvious C^{34}S emission is detected in the dust condensations Nos. 4565 and 4678. No obvious IR cluster is seen in the dust condensation No. 4678.

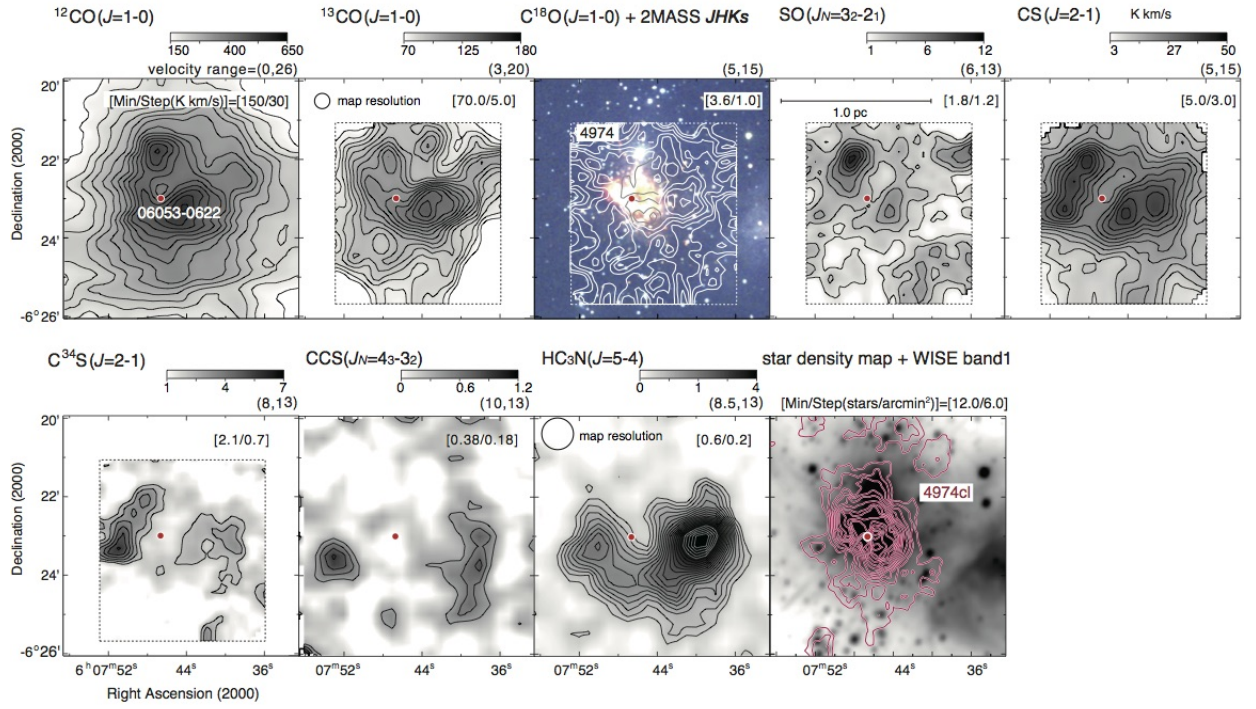
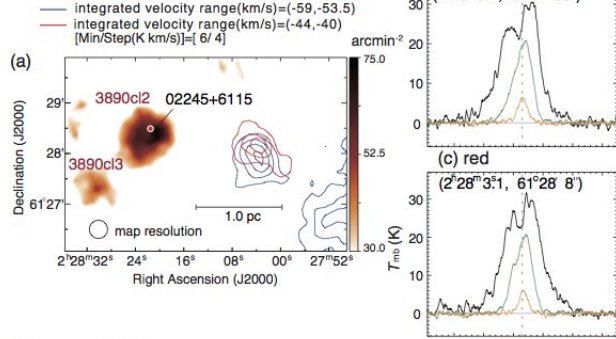
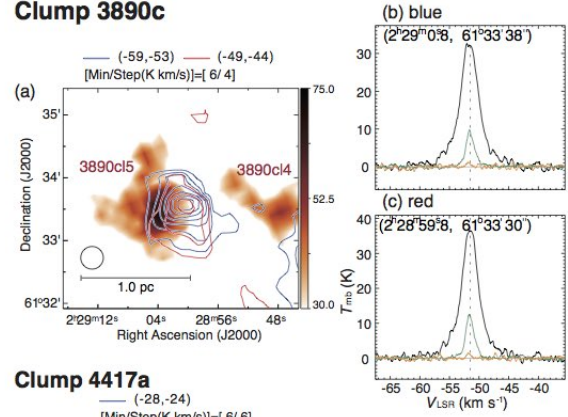
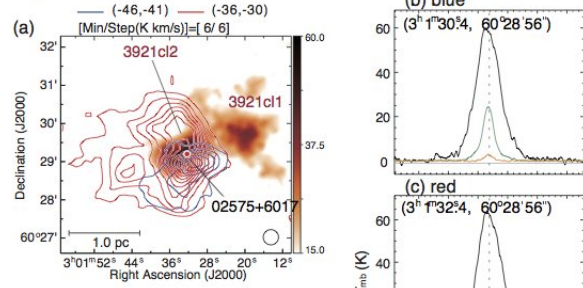
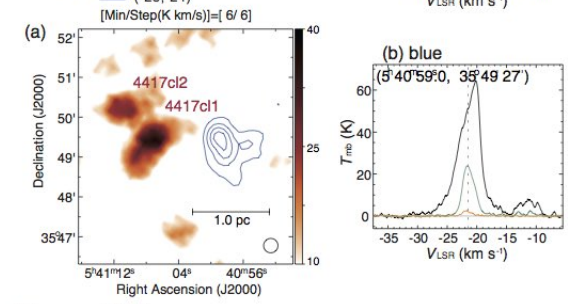
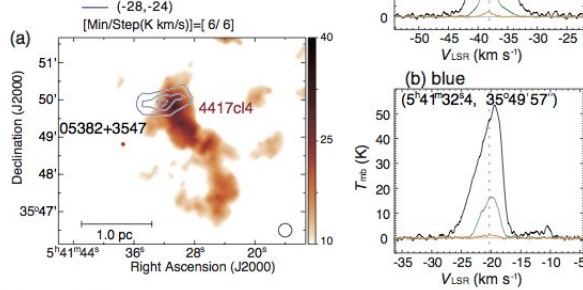
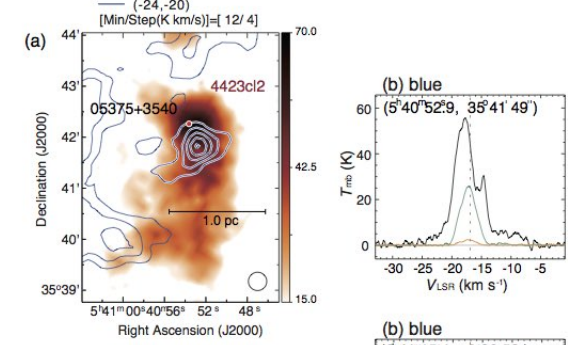
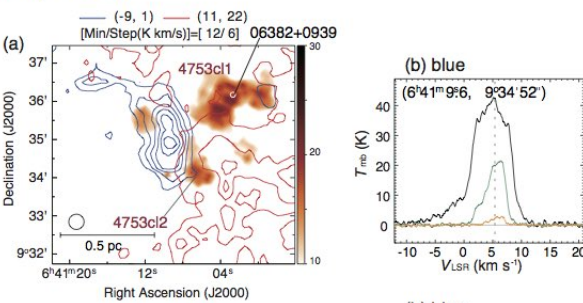
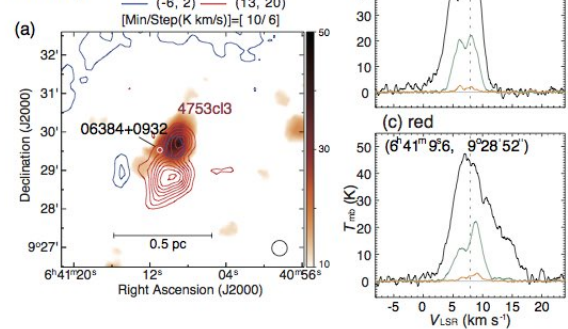
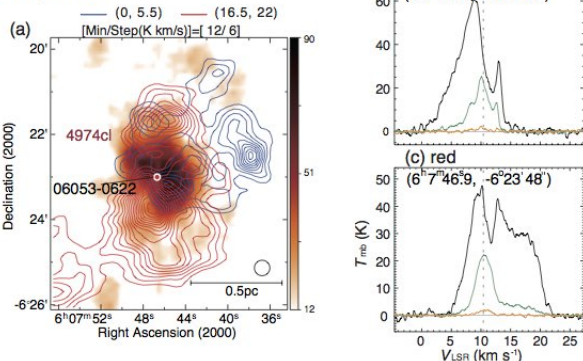
No. 4974

Figure 7. Same as Figure 2, but for the dust condensation No. 4974.

Clump 3890a**Clump 3890c****Clump 3921****Clump 4417a****Clump 4417c****Clump 4423a****Clump 4753a****Clump 4753b****Clump 4974****YSOs**

● IRAS source

contour map

— velocity range : (minimum, maximum) km/s

— contour level : [minimum / contour step] K km/s

spectrum— $^{12}\text{CO} (J=1-0)$ — $^{13}\text{CO} (J=1-0)$ — $\text{C}^{18}\text{O} (J=1-0)$

Figure 8. The ^{12}CO intensity maps for the blue and/or red lobes of the molecular outflows found around the clumps are shown in panel (a). The red scale denotes the star density distributions. The red contours denote the red lobes, and the blue contours denote the blue lobes. The contours start from the 3σ noise level. Sample spectra obtained at the intensity-peaks of the blue lobes and the red lobes are shown in panels (b) and (c), respectively. The equatorial coordinates are given in each panel. The vertical broken line in the spectra marks the systemic velocity.

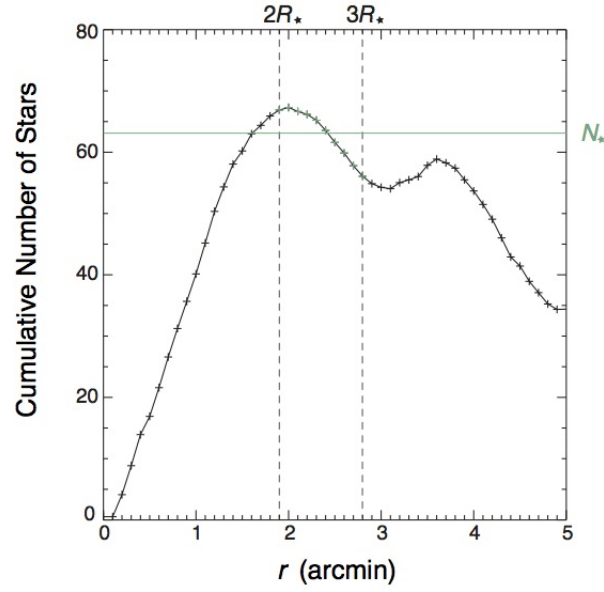


Figure 9. Cumulative number of stars as a function of radius for the cluster 3645cl. The number of stars were measured with the background-subtracted star density map. The number of stars of the cluster N_* (indicated by the green line) was defined as the mean number of stars at $r = 2R_*$ and $3R_*$ where R_* is the cluster radius (see text).

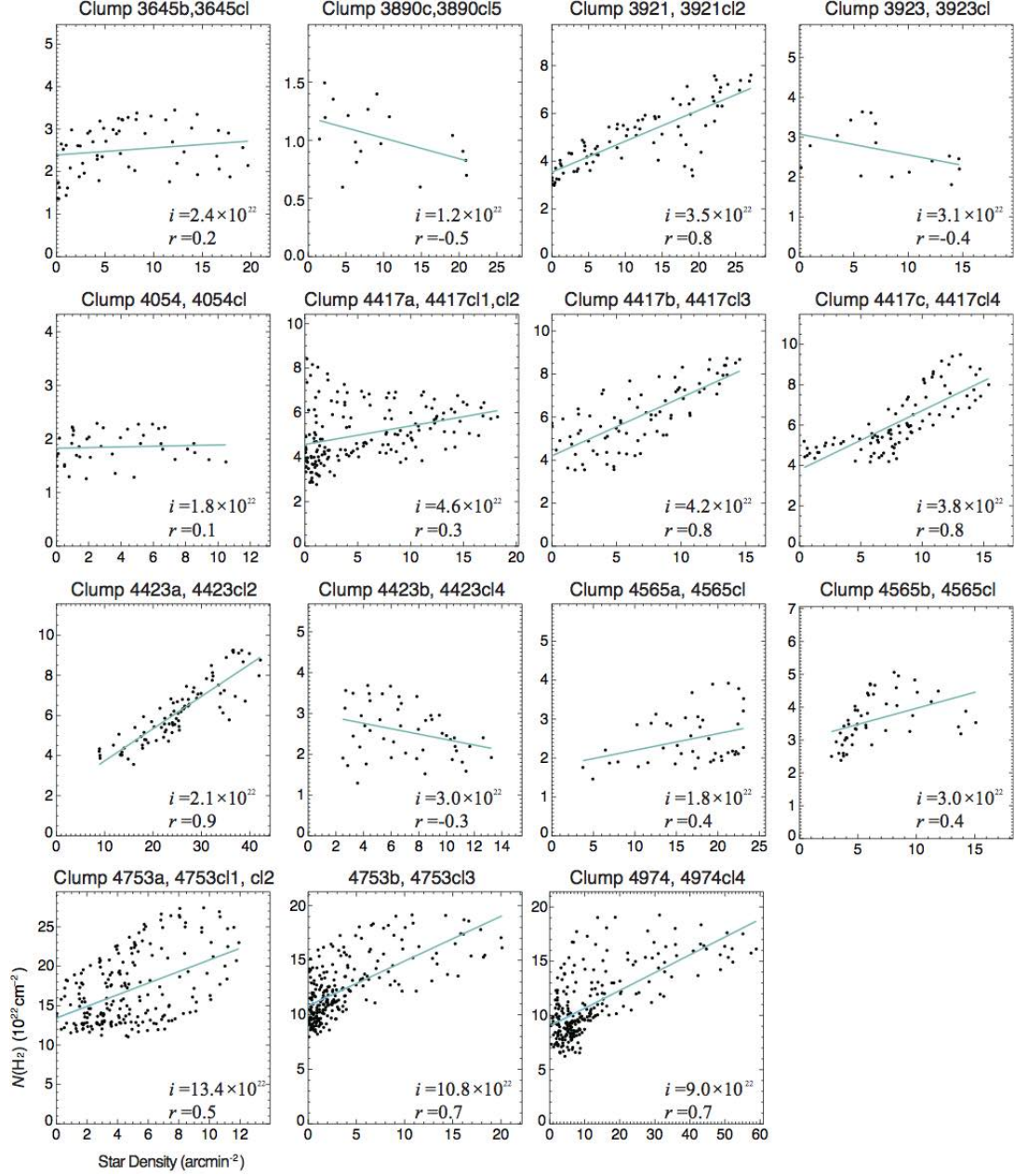


Figure 10. Correlation between $N(\text{H}_2)$ and the star density of the 16 clumps with IR clusters. The blue lines denote the linear least-square fit. The intercepts i and correlation coefficients r for the relations are denoted in the panels.

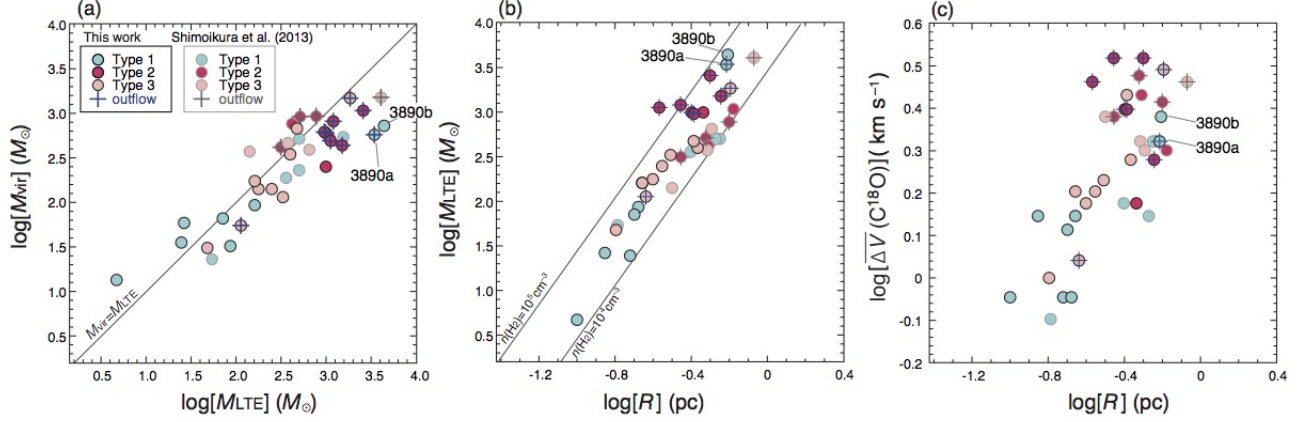


Figure 11. Relation between (a) M_{vir} and M_{LTE} , (b) M_{LTE} and R , and (c) $\overline{\Delta V}(\text{C}^{18}\text{O})$ and R for the 24 clumps. Blue, red, pink circles represent the clumps of the different types. Plus signs denote the clumps associated with a molecular outflow. We also show data points of other clumps presented by Shimoikura et al. (2013).

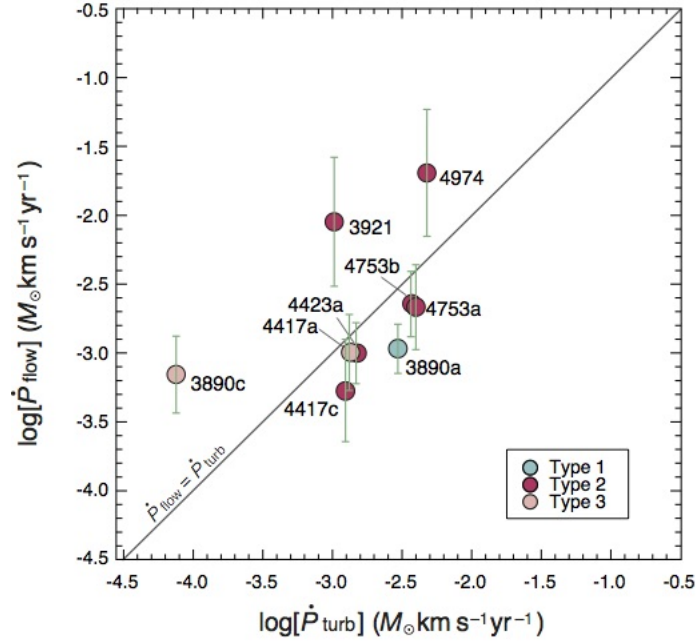


Figure 12. The \dot{P}_{flow} vs. \dot{P}_{turb} relation for the clumps associated with outflows. For \dot{P}_{flow} , we plot the geometrical mean values with error bars (green line) representing the minimum and maximum estimates (see Appendix B).

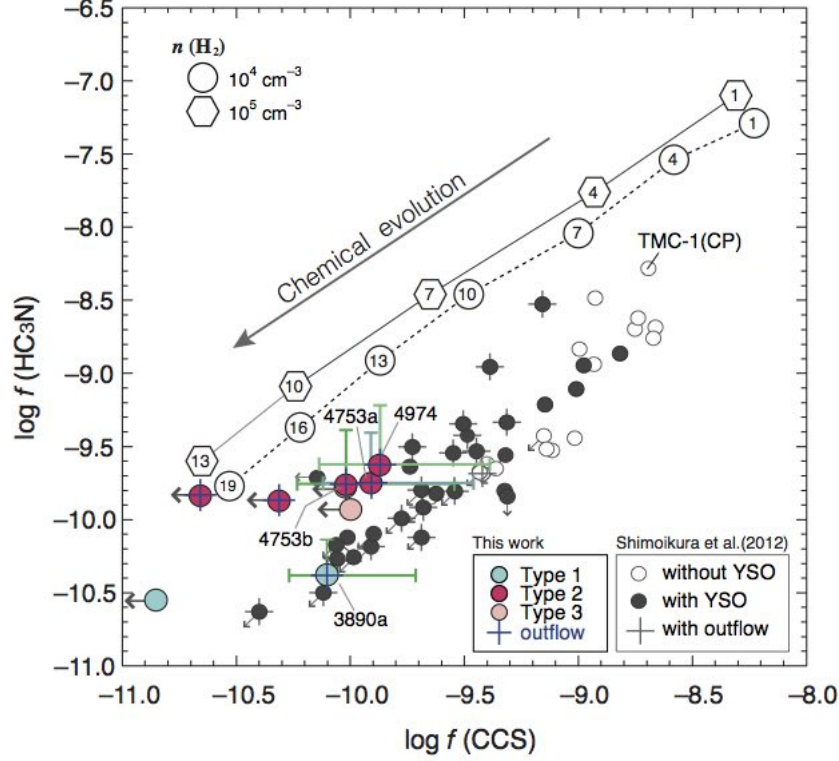


Figure 13. The diagram of $f(\text{HC}_3\text{N})$ vs. $f(\text{CCS})$ of the nine clumps detected in HC_3N , compared with the sample of cores with and without YSOs reported by Shimoikura et al. (2012). The plots are the geometrical mean of the upper and lower limits of $f(\text{HC}_3\text{N})$ and $f(\text{CCS})$ arising from the different assumption of T_{ex} (see text). We show error bars (green line) representing the upper and lower limits only for the clumps detected both in CCS and HC_3N . Arrows indicate the upper limits measured from the noise level. Larger circles and hexagons represent the fractional abundances calculated by (Suzuki et al. 1992, see their Figure 14) for the initial hydrogen densities $n(\text{H}_2) = 10^4 \text{ cm}^{-3}$ and 10^5 cm^{-3} , respectively. Numbers inside the symbols represent the time in units of 10^5 yr from the beginning of the chemical reaction.

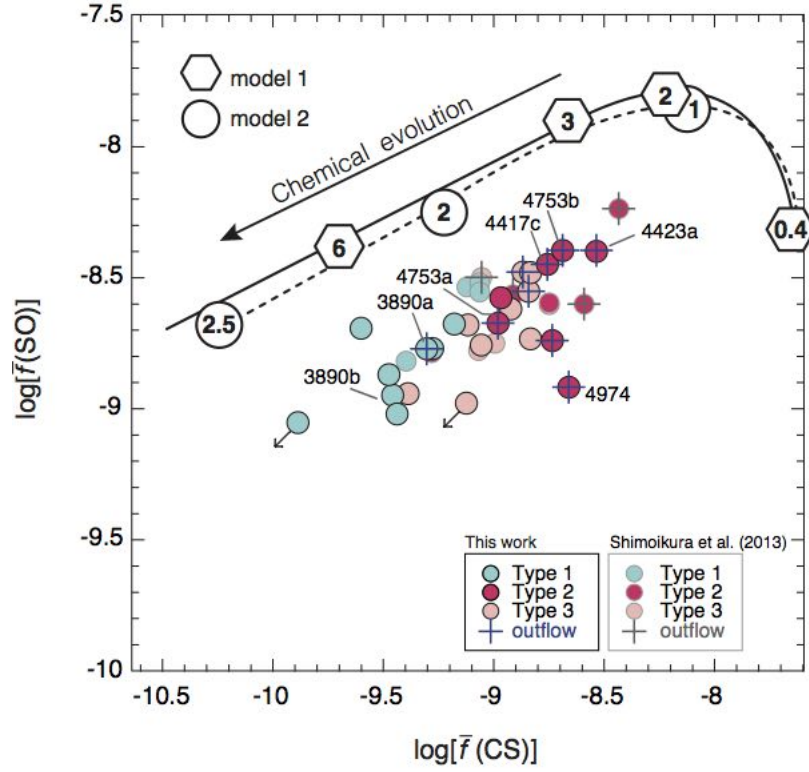


Figure 14. The diagram of $\bar{f}(\text{SO})$ and $\bar{f}(\text{CS})$ of the 24 clumps. We also plotted the clumps presented by Shimoikura et al. (2013). Arrows indicate the upper limits. Larger circles and hexagons represent the fractional abundances calculated for the two different models called model 1 and model 2 by Bergin & Langer (1997, see their Figures 2 and 3). Numbers inside the symbols represent the time in units of 10^6 yr from the beginning of the chemical reaction.

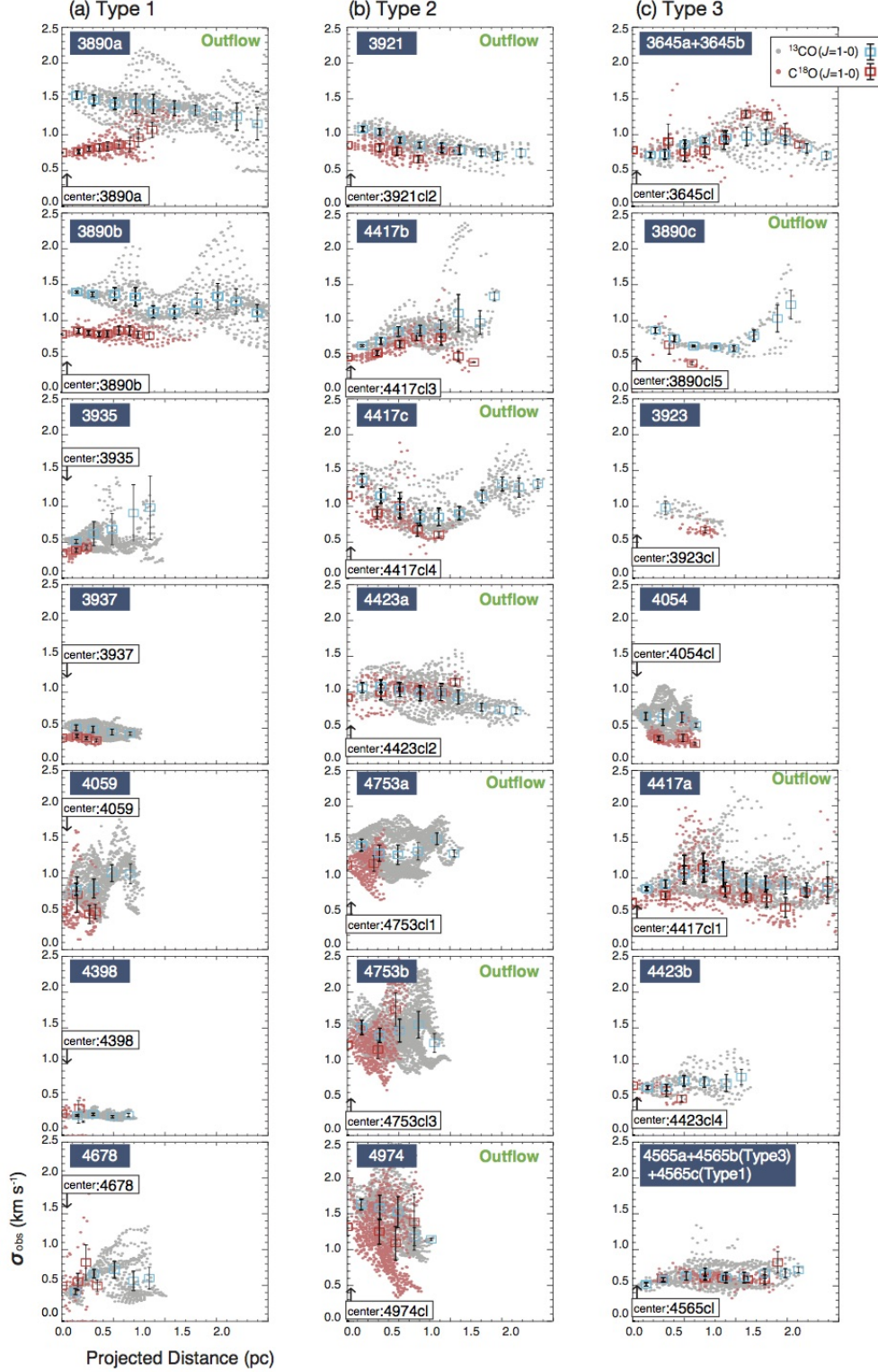


Figure 15. Variation of velocity dispersion (σ_{obs}) for each clump as a function of the distance from the cluster center (for the Types 2 and 3 clumps) or the C^{18}O emission peak position (for the Type1 clumps). The different color dots represent the velocity dispersion values measured from the ^{13}CO (grey) and C^{18}O (pink) data. Blue and red squares represent the median values of σ_{obs} in the 0.2 pc bin for the ^{13}CO and the C^{18}O data, respectively. The error bars show the standard deviation of each data in the bins.

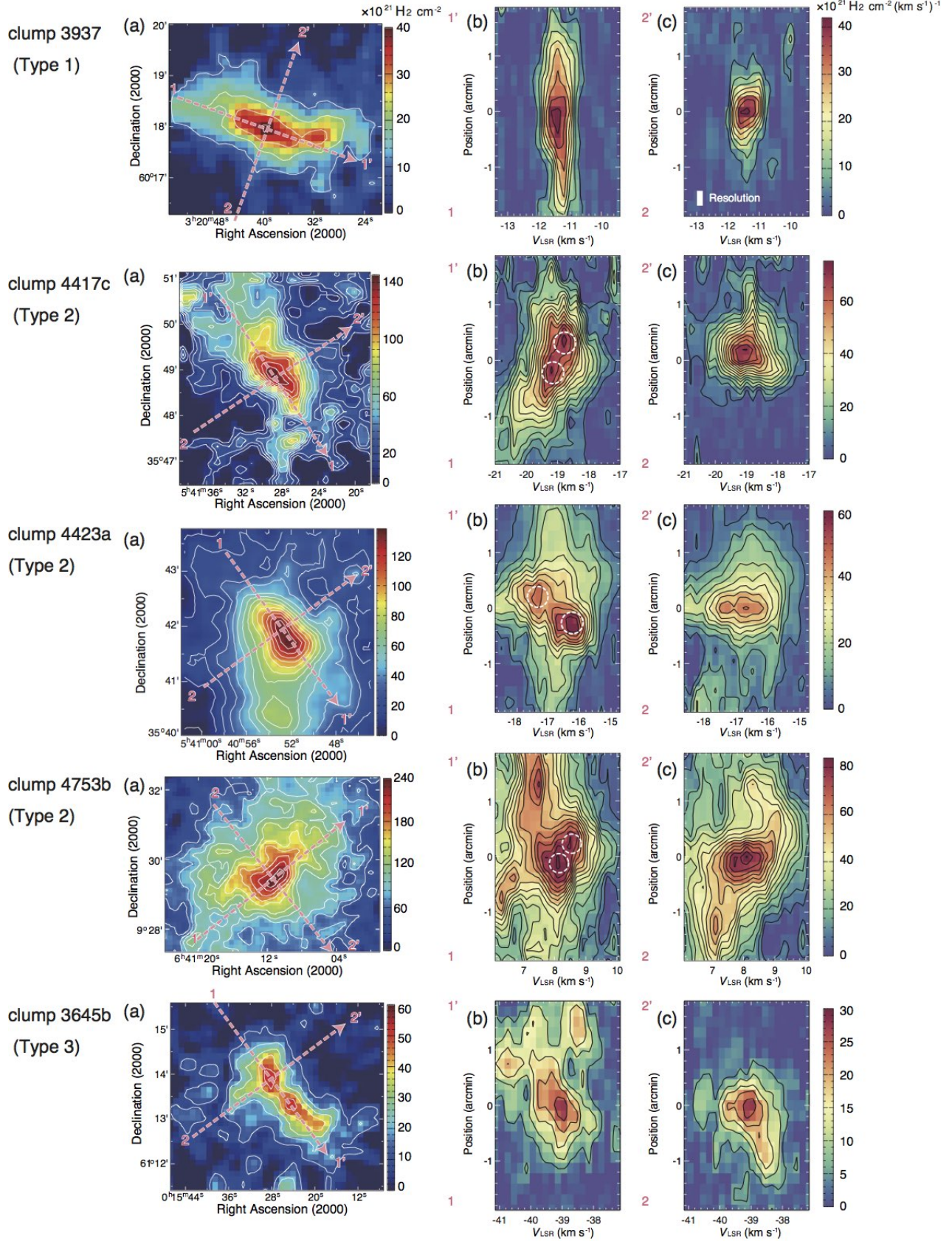


Figure 16. Distributions of the H_2 column density derived from the C^{18}O integrated intensity, observed position-velocity diagram measured along the major axis (cut 1-1'), and that measured along the minor axis (cut 2-2'), are displayed in panels (a)–(c) for clumps classified to Types 1–3. The lowest contour and contour interval for panel (a) are $1 \times 10^{22} \text{ H}_2 \text{ cm}^{-2}$ for all of the clumps except for clump 4753b whose lowest contour and contour interval are $5 \times 10^{22} \text{ H}_2 \text{ cm}^{-2}$ and $2 \times 10^{22} \text{ H}_2 \text{ cm}^{-2}$, respectively. The lowest contour and contour interval for panels (b) and (c) are $5 \times 10^{21} \text{ H}_2 \text{ cm}^{-2} (\text{km s}^{-1})^{-1}$ for all of the clumps. White broken circles in panels (b) for the Type 2 clumps denote the double-peaked feature (see text).

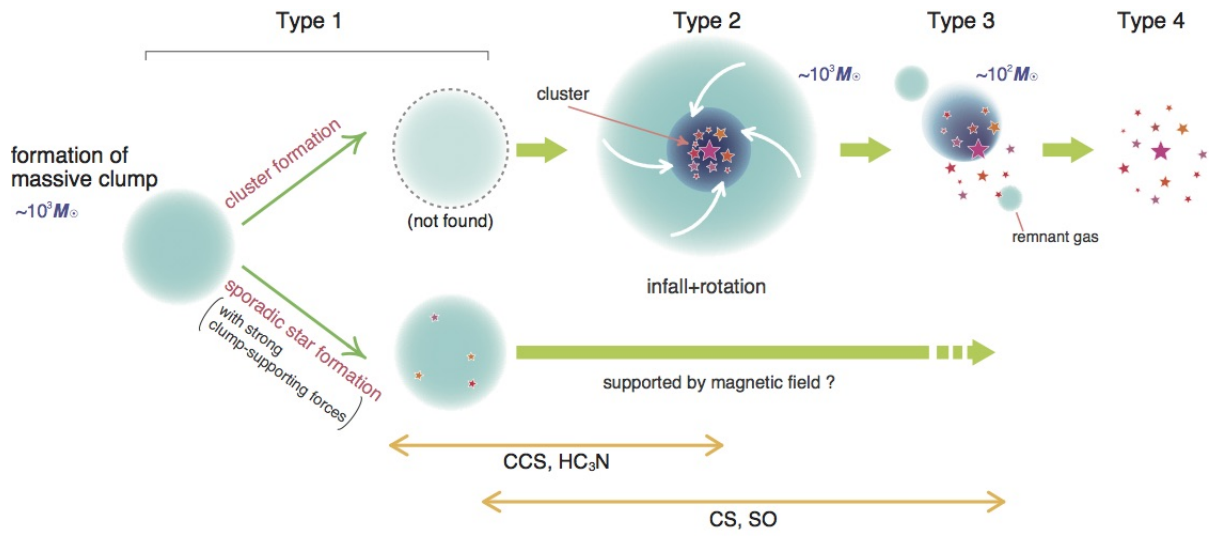


Figure 17. The proposed evolutionary scenario of cluster formation.

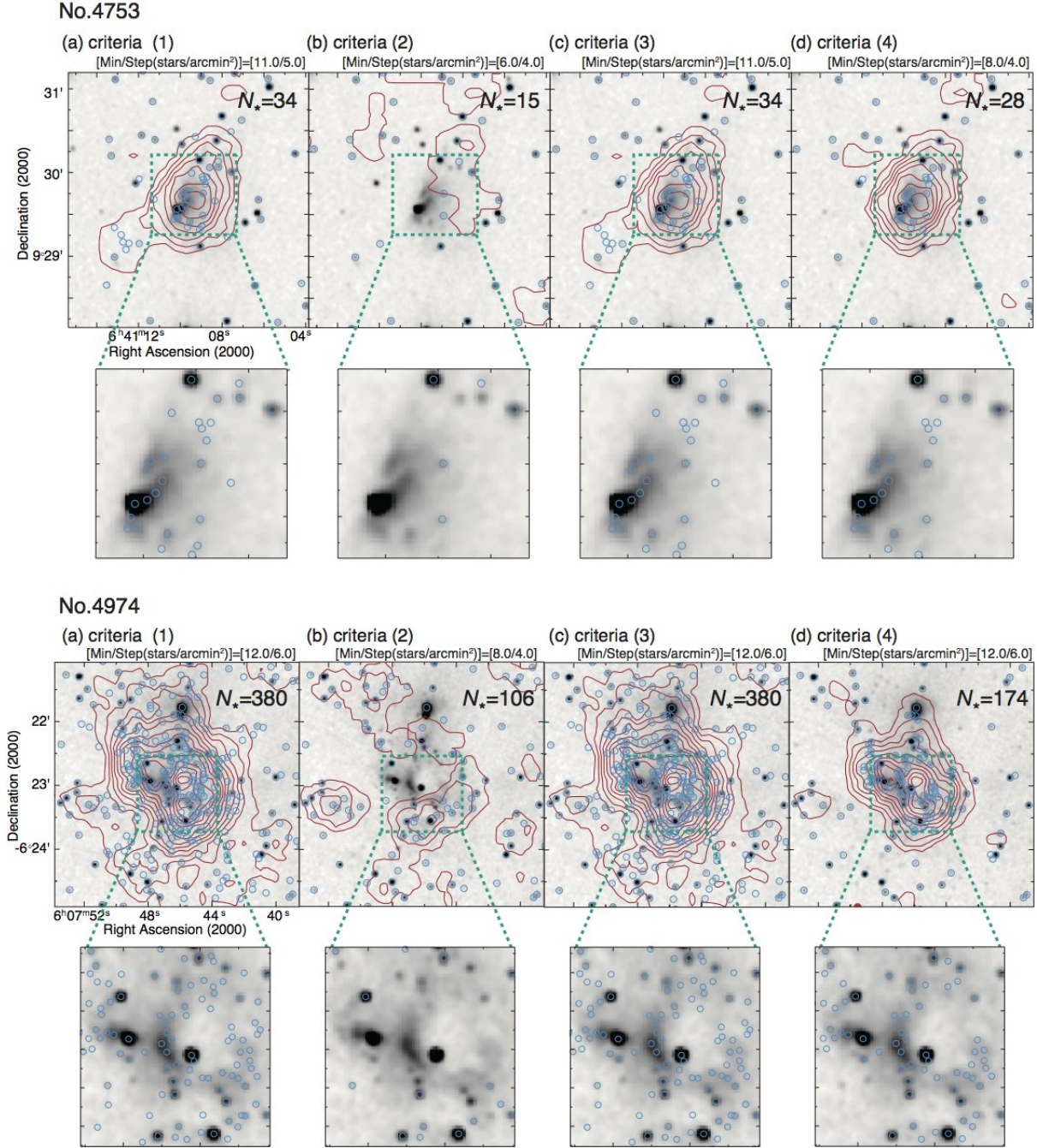


Figure 18. Distributions of stars (blue circles) in the No.4753 and No.4974 regions selected under the selection criteria (1)–(4) in Appendix C. Star densities are shown by the red contours. Close-up views of the central regions are also shown in the lower panels. The background is the 2MASS *J* band image.

APPENDIX

A. DERIVATION OF THE COLUMN DENSITY

The brightness temperature corrected for the main beam efficiency T_{mb} of the observed emission line is given by

$$T_{\text{mb}} = [J(T_{\text{ex}}) - J(T_{\text{bg}})][1 - \exp(-\tau)] , \quad (\text{A1})$$

where τ is the optical depth, $J(T) = T_0/(e^{T_0/T} - 1)$, and $T_{\text{bg}} = 2.7$ K. T_0 is a constant calculated as $T_0 = h\nu_0/k$ where k , h , and ν_0 are the Boltzmann constant, the Planck constant, and the rest frequency of the observed emission line, respectively. On the assumption of the Local Thermodynamic Equilibrium (LTE), column density for the optically thin lines can be obtained with the following equation (e.g., [Hirahara et al. 1992](#)),

$$N = \frac{3h}{8\pi^3} \frac{Q}{\mu^2 S_{ij}} \frac{e^{E_u/kT_{\text{ex}}}}{e^{T_0/T_{\text{ex}}} - 1} \frac{1}{J(T_{\text{ex}}) - J(T_{\text{bg}})} \int \beta^{-1} T_{\text{mb}} dv. \quad (\text{A2})$$

Here, Q is the partition function approximated as $Q = kT_{\text{ex}}/hB_0$ where B_0 is the rotational constant of the molecule. μ is the dipole moment, E_u is the energy of the upper level, and S_{ij} is the intrinsic line strength of the transition for i to j state. β is the escape probability given by $\beta = (1 - e^{-\tau})/\tau$, and $\beta = 1$ for $\tau \ll 1$. The spectral line parameters are taken from Splatalogue⁴, a database for astronomical spectroscopy. We summarize the line parameters used in this study in Table 9.

B. SEARCH FOR OUTFLOWS AND ESTIMATION OF THE OUTFLOW PARAMETERS

In order to search for reliable candidates of outflows, we checked the ^{12}CO spectra if they show blue- and/or redshifted high velocity wings around the center velocity of C^{18}O at each pixel. We also investigated the ^{12}CO distributions based on the PV diagrams which is useful to find outflows and to determine the velocity range of the outflowing gas. In total, we found nine outflows which are shown in Figure 8. We also show some emission lines observed toward the peak position of the high velocity emission.

In Table 6, we provide an estimate of the masses of the outflows M_{lobe} and their properties. We measured the peak positions of the lobes, and also defined the surface area of the lobes S_{lobe} at the 3σ contour level of the maps for each outflow. R_{lobe} is the radius of the lobes calculated as $R_{\text{lobe}} = \sqrt{S_{\text{lobe}}/\pi}$, and V_{sys} is the systemic velocity defined as the peak velocity of the C^{18}O spectra. The maximum velocity shift of the ^{12}CO emission from the systemic velocity, which we call characteristic velocity V_{char} , is defined as $V_{\text{char}} = |V_{\text{sys}} - V_{\text{max}}|$ where V_{max} is the maximum velocity of the high velocity wings detected at the 3σ noise level. We tried to measure the optical depth of ^{12}CO from the ratio of the ^{12}CO intensity to the ^{13}CO intensity. However, there is very little detectable ^{13}CO emission above the noise level within the lobes. We therefore measured the upper limit of the optical depth at the intensity peak position of the lobes, τ_{max} , and derived properties of the outflowing gas for the upper limits.

To estimate τ_{max} , we assumed that the ^{13}CO is optically thin and that the $[^{12}\text{CO}]/[^{13}\text{CO}]$ abundance ratio is equal to the terrestrial value (89) as follows,

$$\frac{I(^{12}\text{CO}_{\text{wing}})}{I(^{13}\text{CO}_{\text{wing}})} = 89 \times \frac{1 - e^{-\tau_{\text{max}}}}{\tau_{\text{max}}}, \quad (\text{B3})$$

where $I(^{12}\text{CO}_{\text{wing}})$ and $I(^{13}\text{CO}_{\text{wing}})$ are the integrated intensity of the ^{12}CO and ^{13}CO emission lines measured at the peak positions of the lobes, respectively.

As the lower limits for the properties of the outflowing gas, we assumed that wing components in the ^{12}CO emission line are optically thin ($\tau \ll 1$).

Using the calculated T_{ex} (see Section 3.1), we derived the ^{12}CO column densities of the outflows $N(^{12}\text{CO})$ from Equation (A2). For the estimation of the upper and lower limits, we used $\beta = (1 - e^{-\tau_{\text{max}}})/\tau_{\text{max}}$ and $\beta = 1$, respectively. The molecular column density $N(\text{H}_2)$ was then calculated from $N(^{12}\text{CO})$, assuming a CO fractional abundance of 1×10^{-4} ([Frerking et al. 1982](#)). Masses of the outflow lobes M_{lobe} were derived from Equation (2) within S_{lobe} .

We list in Table 6 the derived M_{lobe} as well as the momentum $P_{\text{lobe}} = M_{\text{lobe}}V_{\text{char}}$, dynamical timescale $t_{\text{d}} = R_{\text{lobe}}/V_{\text{char}}$, and momentum supply rate $\dot{P}_{\text{lobe}} = P_{\text{lobe}}/t_{\text{d}}$. In this study, we made no attempt to correct for the inclination angle of the outflows.

⁴ www.splatalogue.net

C. CRITERIA TO SELECT STARS BASED ON THE 2MASS PSC

In order to search for IR clusters in this paper, we used all of the stars in the 2MASS PSC except for those identified as minor planets, because most of the cataloged stars are significantly detected at least in one of the 2MASS bands (*JHKs*). However, as pointed out by [Cambr  sy et al. \(2002\)](#), it is known that there are a certain fraction of false stars in the 2MASS PSC around bright stars and nebulae associated with small HII regions. In order to check how much our sample of stars can be contaminated by the false stars, we made a test by applying some tighter criteria and by checking the appearance of the selected stars on the 2MASS images.

The test was made toward the dust condensations No. 4753 (NGC 2264) and No. 4974 (Mon R2) that are known to be accompanied by IR clusters (e.g., [Peretto et al. 2006](#); [Dierickx et al. 2015](#)). We produced star density maps covering a $15' \times 15'$ area around No. 4753 and a $40' \times 40'$ area around No. 4974 using stars selected under the following four different criteria:

- (1) Stars except for those with a minor planet flag.
- (2) Stars satisfying the above (1), and having a photometry quality flag of A, B, or C and a read flag of 1, 2, or 3 in all of the three *JHKs* bands.
- (3) Stars satisfying the above (1), and having a photometry quality flag of A, B, or C and a read flag of 1, 2, or 3 at least in one of the *JHKs* bands.
- (4) Stars satisfying the above (1), and having a catalogued magnitude of $J < 16.0$ mag, $H < 15.5$ mag, and $K_s < 15.0$ mag.

The criteria (1) are what we used in this study, the criteria (3) are to ensure the detection at least in one of the 2MASS bands, the criteria (4) are tighter than these, and the criteria (2) are the tightest.

The results are summarized in Figure 18 where the individual selected stars (blue circles) and star densities (red contours) of the two regions are shown. The 2MASS *J* band image is overlaid in all of the panels. We estimated N_* the number of stars in the two clusters by removing the background based on the 3σ clipping procedure in the same way as described in Section 3.4. The values of N_* are given in the upper-right corner of each panel.

As seen in the figures, in the case of the criteria (2), there are many stars apparently escaped selection because the criteria are too tight, and we cannot even realize the existence of the cluster in the case of No. 4753. In the case of the criteria (3), almost the same stars are selected as the criteria (1). In the case of the criteria (4), the spatial distributions of the clusters (traced by the contours for the star densities) are similar to those derived using the criteria (1), though there are still some apparent real stars which escaped selection and N_* decreases by $\sim 20\%$ and $\sim 60\%$ for Nos. 4753 and 4974, respectively.

In the lower panels of Figure 18, we also show a close-up view of the central regions. There are some stars among those selected with the criteria (1) and (3) which we cannot determine if they are real stars or false detections due to the influence of nearby bright source and lumpy/filamentary structures of the nebula. However, the criteria (1) allow us to select all of the apparent stars in the *J* band images, while the criteria (2) and (4) miss many obviously real stars.

In addition to the above (1)–(4), we also tried the criteria that [Cambr  sy et al. \(2002\)](#), see their Section 3) employed to identify IR clusters in the North America and Pelican nebulae, and found that the resulting stars are similar to those selected by the above criteria (2).

We believe that there is no ideal criteria which can exclude false stars perfectly from the 2MASS PSC in all of the IR clusters, and thus we have to choose realistic criteria to better measure the cluster parameters we want to know. Because we first need to know the existence of clusters and secondly their distributions and extents even roughly, we decided to use the criteria (1) in this paper.